ESTIMATION OF ULTRAFAST LASER-INDUCED STRESS IN FUSED SILICA FROM EVALUATION OF STRESS BIREFRINGENCE

by

Alex St. Peter

A Thesis Submitted to the Faculty of the

JAMES C. WYANT COLLEGE OF OPTICAL SCIENCES

In Partial Fulfillment of the Requirements

For the Degree of

MASTER OF SCIENCE

In the Graduate College

THE UNIVERSITY OF ARIZONA

2023

THE UNIVERSITY OF ARIZONA
GRADUATE COLLEGE

As members of the Master's Committee, we certify that we have read the thesis prepared by **Alex St. Peter**, titled ***Estimation of Ultrafast Laser-Induced Stress in Fused Silica from Evaluation of Stress Birefringence*** and recommend that it be accepted as fulfilling the thesis requirement for the Master's Degree.

Brandon D Chalifoux

Professor Brandon D. Chalifoux Date: 4/27/2023

Professor Meredith K. Kupinski Date: 4/27/2023

Greg A. Smith

Professor Greg A. Smith Date: 4/28/2023

Final approval and acceptance of this thesis is contingent upon the candidate's submission of the final copies of the thesis to the Graduate College.

I hereby certify that I have read this thesis prepared under my direction and recommend that it be accepted as fulfilling the Master's requirement.

Brandon D Chalifoux

Professor Brandon D. Chalifoux Date: 4/27/2023
Master's Thesis Committee Chair
Wyant College of Optical Sciences

Acknowledgements

It is my pleasure to offer my sincere gratitude to Dr. Brandon Chalifoux for his guidance and encouragement throughout my college career. His genuine interest in my success as a student and researcher has empowered me to push through academic challenges, broaden the limits of my understanding, and learn to enjoy each step along the way. It has been an honor to be a part of his Lightweight Optics Laboratory, and to make some academic contribution to the discoveries made there.

I also thank and acknowledge Dr. Greg Smith for his key contributions to the research presented in this thesis. His guidance during the creation of the imaging polarimeter was invaluable, and I sincerely appreciate the time he put towards working through challenges alongside me, as well as the unique perspectives he provided during my research.

I am also extremely appreciative of Dr. Meredith K. Kupinski for the polarization expertise she shared with me as I worked on this research. Her academic prowess is admirable, and I more than appreciate her passion for polarization and her ability to share that with others.

Finally, I'd like to share my gratitude for my wife and family who have cheered me on each step of the way. Thank you.

Table of Contents

List of Figures

Abstract

Ultrafast laser stress figuring (ULSF) is capable of deterministically modifying low-spatial frequency height of thin mirrors, without creating higher-spatial frequency errors by generating stress using focused ultrafast laser pulses. The permanent stress field caused by sub-picosecond laser pulses varies in both profile and magnitude depending on pulse parameters and material properties, and results in stress birefringence. Ultrafast laser pulses also generate nanogratings, causing form birefringence in the modification region. The ability to visualize and quantify the birefringence from these stress fields and nanogratings allows for higher precision figuring as well as an understanding of the polarization effects caused by ULSF at high spatial frequencies. This thesis demonstrates the ability to visualize these stress fields through single shot polarization microscopy. Our procedure makes use of division of focal plane (DoFP) imaging to measure fields of birefringence surrounding laser-induced modifications created through ULSF. We do so by propagating near monochromatic circularly polarized light through a modified sample to a DoFP camera and use the subsequent intensity data to output the local stress birefringence at each pixel. We then demonstrate the creation and use of a finite element model to simulate both the form and stress birefringence generated in laser-induced modifications. We then attempt to compare experimental measurements to those generated in the finite element model of the laser-induced modification to infer the stress state in the modification itself. The proposed imaging polarimeter allows for quantification of the extent and magnitude of these stress fields, which will improve the precision of the ULSF process.

Chapter 1 – Introduction

1.1 Motivation and Ultrafast Laser Stress Figuring Background

Ultrafast laser stress figuring is a fabrication process used to produce freeform glass surfaces by modifying the spatially variant curvature of a mirror by applying deterministic stress to its substrate to impart a stress-induced bending moment[1]. This process allows for accurate figuring of thin optics without causing mid-spatial frequency (MSF) error[1] through the creation of approximately ellipsoidal modifications within the substrate.

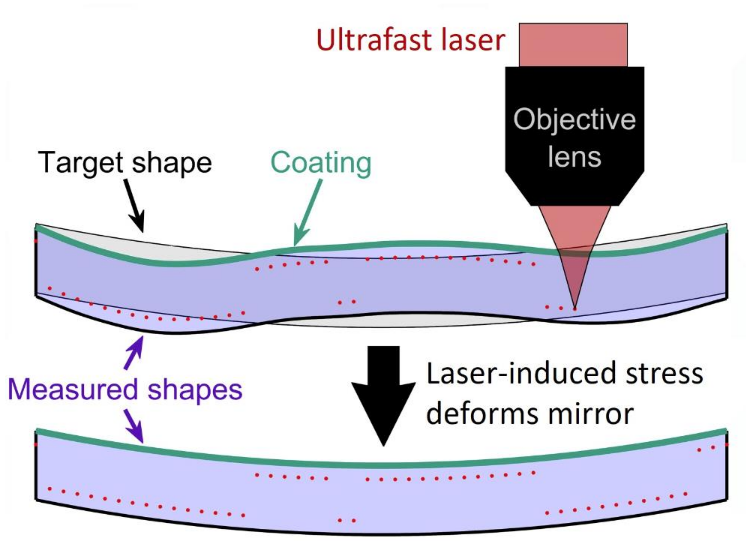

Figure 1: ULSF is performed by focusing laser pulses into the substrate at various depths to cause stresses which deform the material in a predictable way such that the unfigured substrate matches the predetermined target shape[1].

These modifications are created as ultrafast laser pulses ionize a large number of electrons, transferring energy into the material. Ultrafast lasers are useful as they generate high intensity, tightly focused pulses with enough energy to overcome the electric field that binds the valence electrons in an atom[2]. This is important as this causes nonlinear absorption, making it possible to confine the absorption to the focal volume inside the material without causing absorption at the surface. Furthermore, sub-picosecond laser pulses are ideal as the timescale over which the electrons are excited is smaller than the electron–phonon scattering time[2]. This means that each ultrafast laser pulse finishes before the electrons thermally excite any ions, minimizing heat diffusion, which leads to higher precision figuring[3]. While the distribution of stress within the ellipsoidal inclusions generated from ultrafast laser pulses is generally uniform[4], the stresses surrounding modifications vary widely due to many parameters such as laser pulse duration, modification count, laser energy, numerical aperture, and substrate material properties. The stress generated from focusing sub-picosecond laser pulses into fused silica causes stress birefringence. Furthermore, ULSF at particular frequencies leads to the formation of self-organized planar nanocracks known as nanogratings, which induce form birefringence within the modification itself[5]. The ability to visualize and quantify the birefringence from these stress fields and nanogratings at micron level allows for higher precision figuring. As many parameters contribute to the stress magnitude and extent, such a capability allows for rapid characterization and understanding of these parameters and the role they play in stress formation. Furthermore, birefringence quantification at the micron level leads to an understanding of some of the polarization effects caused by ULSF at high spatial frequencies. While such polarization effects may not have a significant effect on reflective applications as figuring is done below the reflective surface, they will have an effect on polarization sensitive optical components used in transmission and should therefore be quantified. As such, the spatially variant stress birefringence in a material should be well known to understand that component's various polarization contributions.

1.2 Birefringence Theory

Birefringence is a phenomenon in which a material exhibits different refractive indices depending on the orientation of polarization of incident light. Therefore, the fully defined optical properties of birefringent materials must also take into account the direction of the light's polarization[6]. This is in contrast to isotropic materials, whose optical properties are insensitive to polarization orientation. In many cases, birefringence occurs due to an inherent molecular structure anisotropy, which is found in many crystals such as calcite. However, birefringence can also occur in isotropic materials due to external forces, vibration, pressure, or temperature change experienced by the material. These forces cause internal stresses, which are oriented along a particular direction depending on the orientations of the forces and material. Such stresses induce strain, which is the resulting deformation of the material caused by internal molecular movement. This results in a dimensional change within the material, which in turn modifies the refractive index along that direction. This leads to a difference in refractive indices along two particular directions, resulting in stress birefringence. This stress birefringence affects the wavefront and point spread function of many optical systems[6]. Birefringence can also occur in periodic nanostructures such as laser written nanogratings which exhibit a linear birefringence that is strongly related to the laser polarization[7].

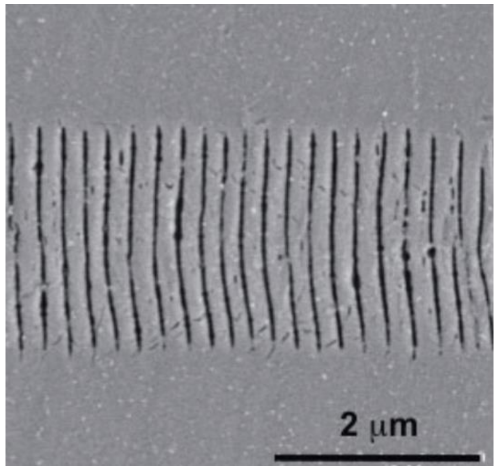

Figure 2: Scanning electron microscope (SEM) image of nanograting formation in fused silica formed from horizontally polarized laser pulses[5].

This is known as form birefringence, which is caused by structure elements such as alternating plates or a regular array of rods having a different refractive index than the bulk material[8]. In the case of fused silica, these nanogratings form from laser pulses due to ultrafast decomposition of silica[9]. Both the form and stress birefringence have an effect on an overall birefringence measurement in the material, and a portion of this paper will focus on our current efforts in decoupling these two effects. As birefringence is a difference in indices of refraction along different light orientations, light consisting of two orthogonal polarization components will experience retardance in a birefringent medium. Retardance is the phase difference between orthogonal polarization components corresponding to the optical path difference the light experiences when passing through a birefringent medium. In general, a simple equation can be used to relate retardance to birefringence using known material parameters, assuming uniform birefringence along the propagation direction.

$$\delta = \frac{2\pi}{\lambda} \Delta \mathrm{n} * t \tag{1}$$

The symbol δ is used to describe retardance in radians, Δn is the birefringence of the material, and t is the distance the light propagates through the birefringent material. Therefore, if the retardance experienced by any particular light ray is known, the birefringence of the material through which it propagated can be readily calculated. An effective way to measure retardance experimentally is to use a polarimeter.

1.3 Imaging Polarimetry Background

A polarimeter is an optical instrument used to measure the polarization properties of light passing through a particular sample or region. While there are multiple types of polarimeters, many use a polarization generator and a polarization analyzer. The generator produces light and then uses polarization components to convert it to a known polarization state. This light then propagates through a designated sample or region of interest before then interacting with an analyzer. The analyzer is another polarization component following the measured sample that converts light to a known polarization state before then performing some form of flux measurement. Generally, the output from multiple analyzers or multiple analyzer configurations is required to determine all the polarization properties of the sample or region of interest being measured as different input polarization states interact differently with various samples. By completing a variety of measurements, the polarization properties of light propagating through the sample of interest can be fully defined using the Stokes vector:

$$S = \begin{pmatrix} S_0 \\ S_1 \\ S_2 \\ S_3 \end{pmatrix} = \begin{pmatrix} P_H + P_V \\ P_H - P_V \\ P_{45} - P_{135} \\ P_R - P_L \end{pmatrix} \tag{2}$$

This requires an understanding of the output horizontal, vertical, 45°, 135°, left circular, and right circular polarized light from the analyzer. However, as seen in equation 3 only a few of these parameters need to be actively measured when the assumption is made that noise present in the system is negligible[6].

$$P_H + P_V = P_{45} + P_{135} = P_R + P_L \tag{3}$$

Therefore, a polarimeter can completely measure the Stokes vector of light using as little as four measurements. The most basic form of polarimeter is the linear polariscope, which is a simple pair of linear polarizers with a sample placed in between them. However, this is not considered a complete polarimeter, as even with the linear polarizers placed in various configurations, the circular polarization component of light remains unknown. There are many other types of polarimeters which each use a different technique to determine various polarization properties. These are time-sequential polarimeters, modulated polarimeters, division of aperture polarimeters, division of aperture polarimeters, and imaging polarimeters[6]. The imaging polarimeter is of highest interest for our research, as it is valuable to image birefringence of laser-induced modifications at a variety of depths, locations, and fields of view in a number of fused silica samples. Imaging polarimetry is the process of determining the polarization state of light, either partially or fully, over an extended scene[10]. An imaging polarimeter makes use of a focal plane array to measure polarization components pixel by pixel. These types of polarimeters generally experience erroneous polarization artifacts due to pixel misalignment between images. One method to account for this is to combine the division of aperture method with an imaging polarimeter, such that only a single shot must be taken to account for all analyzer configurations at once. However, these complex polarimeters still experience a number of inherent errors, and the ones most pertinent to our research will be addressed in section 4.2. While division of aperture imaging polarimeters are useful for rapidly observing polarization properties for a number of imaging scenarios, many of these polarimeters are considered incomplete as they generally cannot measure the circular component of polarization of light. While there are complete Stokes imaging polarimeters[10] the DoFP camera used in our polarimeter employs analyzers whose outputs are 0°, 45°, 90°, or 135° linearly polarized light. As such, the S_3 component of the Stokes vector cannot be determined. However, as our application is purely utilized for stress birefringence measurement, only an understanding of the linear retardance produced by the sample is of interest. Using this analyzer configuration, the retardance at each pixel can readily be calculated when the assumption is made that the magnitudes of depolarization and diattenuation in the sample are negligible.

1.4 Objective

The objective of this thesis is to present a method for stress and form birefringence measurement in laser-induced modifications and their surrounding medium through the construction and use of an imaging polarimeter. These measurements are to be used to quantify the stress fields produced by the laser induced modifications. We present this method and the theory surrounding it to comprehensively describe how stress measurement results are achieved as well as the pertinence of these results in improving ULSF. Our goal is to lay the foundation for accurate stress field measuring using birefringence measurements as well as finite element analysis simulation. We aim to relate the FEA results achieved to experimentally generated data to begin to produce a method for extrapolating stresses due to modification formation and laser polarization orientation separately. The overall objective for this technique is to better understand the stresses produced by laser-induced modifications created through a variety of laser parameters, such that the ULSF technique can be refined to figure mirrors and other substrates more accurately and efficiently.

Chapter 2 – Stress Birefringence Measurement

2.1 *Polarization Microscopy*

In order to measure the stress birefringence in laser pulse induced modifications in substrates, we designed and constructed a polarimeter through modification of an Olympus BX-51 microscope.

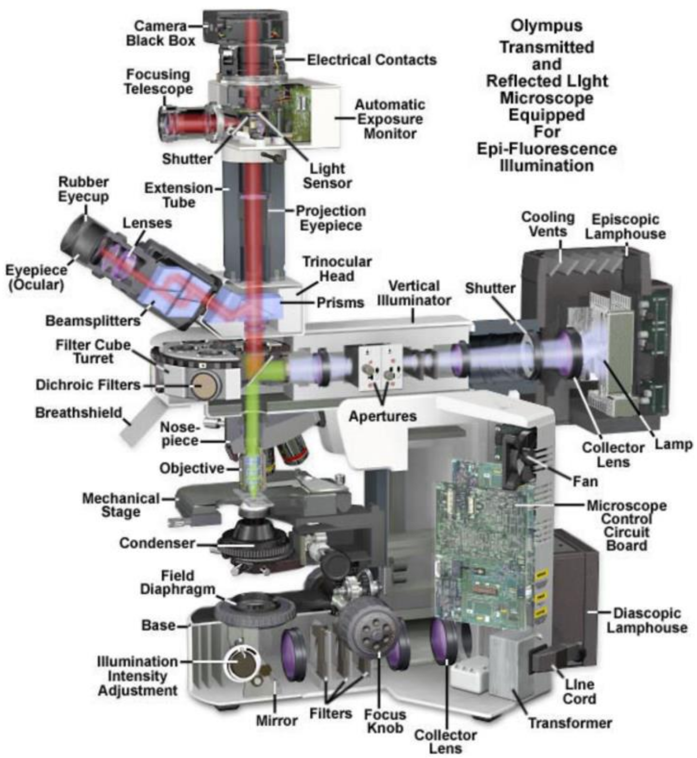

Figure 3: Cutaway view of an Olympus BX-51 microscope showing components and light path for viewing an object in reflection mode[11]. Transmission mode imaging makes use of the lower light source.

This microscope is very modular and has been used in a variety of configurations for a number of research purposes in our lab, making it a suitable candidate for imaging polarimetry. The use of a microscope allows for birefringence measurements to be performed using a number of magnifications and fields of view to allow for comprehensive examination of various modification patterns and sizes in a single run. A number of alterations were required to transform this microscope into an accurate polarimeter. As noted in equation 1, retardance is a function of wavelength. Therefore, using any light source with a broad bandwidth would lead to inaccurate measurements, as the final retardance would need to be integrated across the entire spectrum in use. To eliminate this issue, a 632 nm filter[12] was placed at the output of the 100 W halogen light source, reducing its initial extended bandwidth down to a full width half max bandwidth of 10 nm centered around 632 nm. Due to the inherent configuration of the BX-51 microscope in transmission mode, the near-monochromatic light then reflects off a mirror before propagating to the circular polarizer. The partial polarization produced by reflection is negated by the introduction of a circular polarizer, designed for 632 nm light, located directly after the mirror along the path of propagation in roughly collimated space. The circular polarizer functions by combining a linear polarizer with a quarter wave plate for 632 nm light as shown in figure 4.

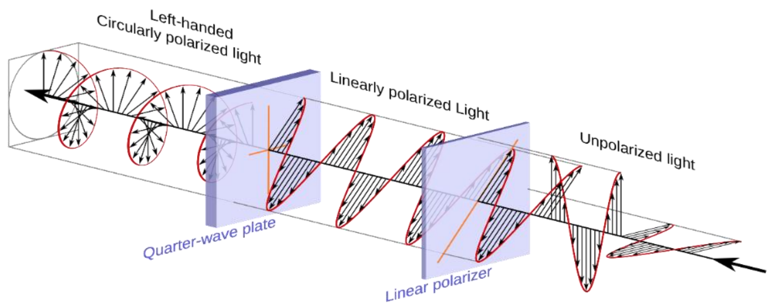

Figure 4: General configuration of a circular polarizer. Circular polarizers consist of a linear polarizer followed by a quarter-wave plate oriented 45° from the orientation of the linear polarizer to generate circularly polarized light regardless of input polarization state[13].

The mathematical derivation demonstrating the polarization effects of this and all other components in the system is further elaborated on in section 2.2. The near-monochromatic circularly polarized light then propagates through a transmissive sample containing the laser pulse induced modifications. The stress birefringence caused by these modifications will introduce retardance to the circularly polarized light. Therefore, any rays passing through these regions of birefringence will become elliptically polarized to some extent. The degree of polarization ellipticity is directly related to the magnitude of birefringence experienced by the ray. Furthermore, both the stress and form birefringence within the modification itself will contribute to the retardance experienced by rays passing directly through the modification. After passing through the sample, light is then collected by an objective and imaged onto the camera detector plane for observation and post-processing. The camera used is the Lucid Triton division of focal plane (DoFP) camera which utilizes a lenslet array to reduce crosstalk between pixels. A DoFP camera is exceptionally useful for rapid single-shot polarization imaging due to the configuration of linear polarizers over each pixel in the focal plane[14].

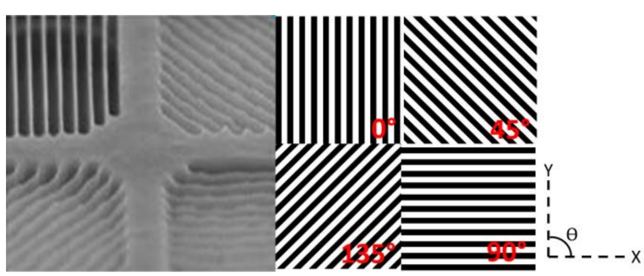

Figure 5: (Left) SEM image of wire grid polarizers situated to form one super-pixel of the Lucid Triton camera[14]. (Right) Representation of the wire grid linear polarizer and the orientations of polarization allowed to pass through each wire grid relative to the given coordinate frame.

As seen in figure 5, a mask of four linear grid polarizers is placed over each super-pixel, and each polarizer is oriented at either 0°, 45°, 90°, or 135°. Using these four polarizations, the entire linear retardance profile of the modified sample can be obtained using a single image and no moving parts. The modified BX-51 microscope with all necessary components including the DoFP camera is shown in figure 6.

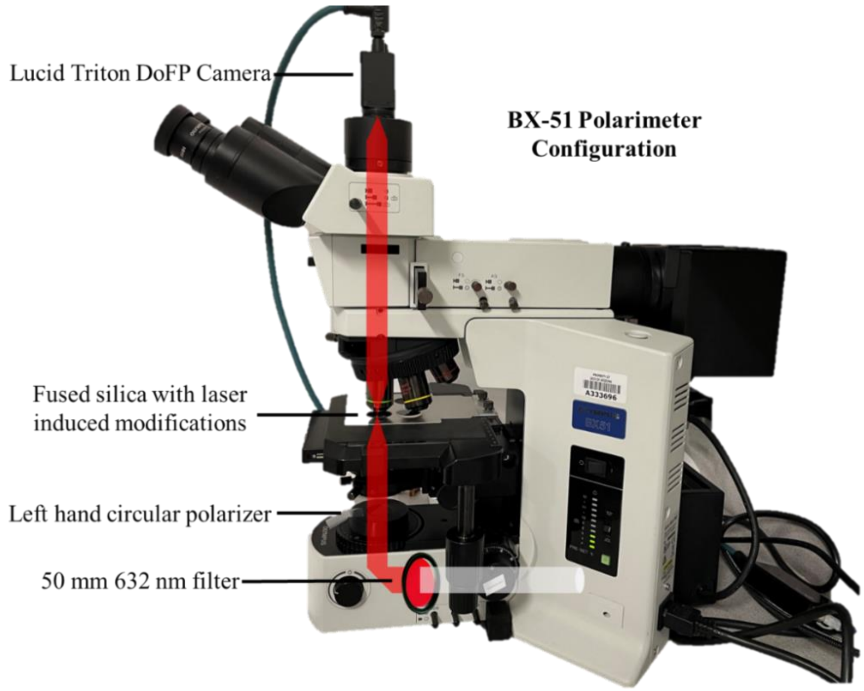

Figure 6: Olympus BX-51 microscope modified to perform as a DoFP imaging polarimeter.

An important note to make regarding the BX-51 microscope (and many others), is that imaging is performed using Kohler Illumination. Kohler Illumination provides uniform and bright illumination over the field of view, even for light sources that are not uniform[15], such as the halogen source used by the microscope. This also ensures that the image of the light source is not focused directly onto the focal plane of the camera. Figure 7 shows a general Kohler Illumination configuration similar to the BX-51 illumination path.

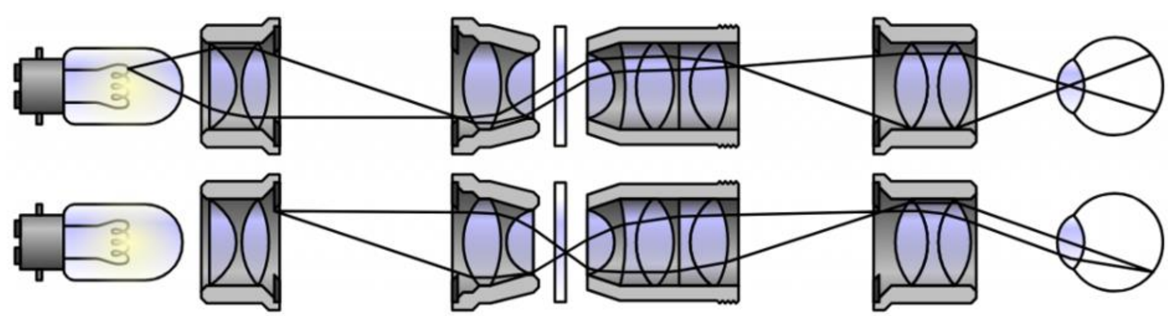

Figure 7: Kohler Illumination demonstration. The imaging system is configured such that light from the source uniformly fills the detector plane while light in the object plane comes to a focus at the detector[16].

While Kohler Illumination is useful for providing uniform illumination across the entire modified region, it also lends itself to high numerical aperture for maximum illumination angular extent to improve image resolution. While this is generally useful for most imaging scenarios due to the increased resolution it provides, such an illumination configuration can cause extreme polarization characterization uncertainty, causing unintended diattenuation as circularly polarized light passes through the imaging optics and sample at high angles of incidence. As shown in figure 8, the magnitude of diattenuation depends entirely on the angle of incidence between the light ray and the curved surface of the objective.

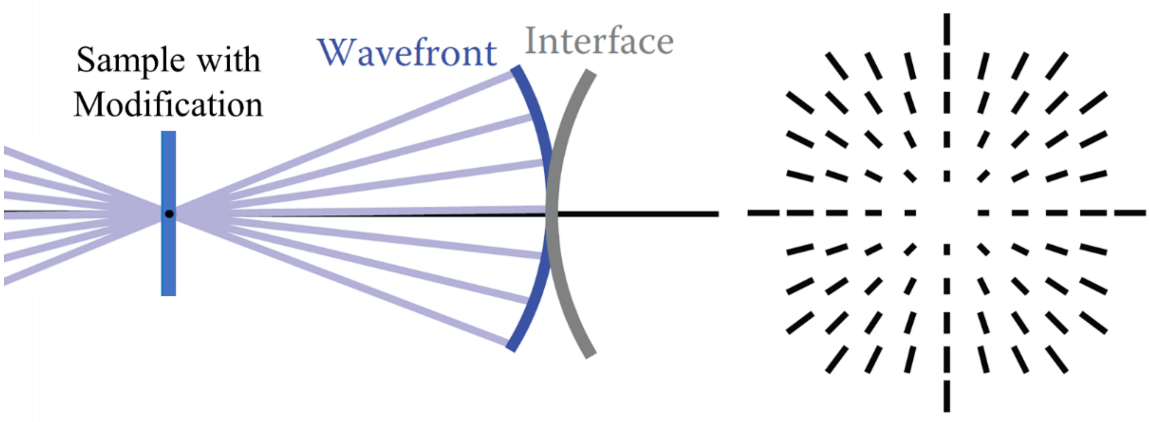

Figure 8: (Left) Rays passing through a sample with a single modification at some arbitrary maximum angle of acceptance. (Right) Relative map of diattenuation caused by the increase in angle of incidence at the refractive interface. Figure adapted from "Polarized Light and Optical Systems"[6].

An effective method to reduce these effects is to significantly decrease the size of the aperture stop. A decrease in aperture stop diameter decreases the angle of acceptance, reducing polarization aberrations. Due to the thickness of the sample, an increase in angle of acceptance leads to an increase in uncertainty regarding the average polarization state of rays hitting each detector pixel. This is especially of concern if additional modifications are made in the substrate above or below the modification of interest as these may affect the retardance of some (but not all) rays focused onto a single detector pixel. This is best demonstrated in figure 9, showing that a larger cone of light increases ray path uncertainty in the substrate directly above or below the modification of interest.

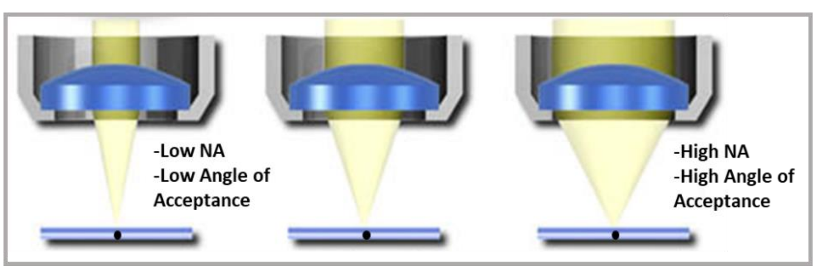

Figure 9: Representation of various numerical aperture (NA) settings to demonstrate the increase in angle of acceptance of rays passing through the modification with an increase in NA[17].

Ideally, the bundle of rays incident on each detector pixel would be collimated in sample space, such that the paths traveled by each ray at an individual location on the detector would be identical. Decreasing the angle of acceptance by as much as possible decreases ray path difference between rays passing through the same focal point and ensures that all rays hitting a single detector pixel experience the same retardance. While decreasing NA reduces the total amount of light propagating through the system, it is necessary to ensure accurate retardance measurement at each location in the imaging plane. The experimental effect of decreasing NA is demonstrated in section 2.3.

2.2 Mathematical Derivation of Polarimetry Technique

The polarimetry technique described in section 2.1 is possible thanks to the Jones matrix and vector characterization of polarization elements and polarized light. The Jones matrix provides a powerful method to describe sequences of polarization elements and the intrinsic polarization properties of ray paths through optical systems[6]. The Jones vector, on the other hand, provides a simple yet effective method of describing polarized light as a vector that sequentially interacts with each of these polarization elements. By performing matrix multiplication, an arbitrary Jones vector corresponding to incident polarized light E_{in} can be multiplied by a series of Jones matrices J_n representing various system elements to output the polarization state of the exiting polarized light E_{out}.

$$E_{\mathrm{out}} = J_n \ldots J_2 J_1 E_{\mathrm{in}} \tag{4}$$

The Jones matrix contributions from each element in a system can be combined into one matrix and the total Jones calculus can be expressed as shown in equation 5:

$$\begin{pmatrix} E_{x,\mathrm{out}} \\ E_{y,\mathrm{out}} \end{pmatrix} = \begin{pmatrix} J_{\mathrm{xx}} & J_{\mathrm{xy}} \\ J_{\mathrm{yz}} & J_{\mathrm{yy}} \end{pmatrix} \begin{pmatrix} E_{x,\mathrm{in}} \\ E_{y,\mathrm{in}} \end{pmatrix} \tag{5}$$

Note that the Jones calculus presented here is done using an x-y basis for convenience. In other words, the Jones vectors presented represent the phase and amplitude of the electric field in the x and y directions. An important assumption used in this application of Jones calculus is that the incident light is fully polarized, and that no depolarization occurs during propagation, as Jones calculus does not account for this effect. For our application, this is a valid assumption as we are only looking to observe effects due to stress birefringence, which is mainly captured in retardance. Furthermore, none of the optical components in this microscope configuration induce significant depolarization. This assumption is validated in section 4.2. While the presented polarimeter configuration consists of a number of optical elements, only those whose Jones matrices introduce a significant polarization effect will be used for retardance and fast axis angle calculations. These are namely the circular polarizer, the modification itself, and the linear polarizers in the camera focal plane. As retardance magnitude is related to the magnitude of stress birefringence, and the retardance orientation is associated with the orientation of the principal stresses, these are the two values of importance for calculation. Equations 6 and 7 outline the pertinent Jones matrices and vectors relating to the optical elements which introduce a significant polarization in our polarimeter setup.

$$E_{\text{out}} = J_{\text{LP}} J_{\text{sample}} J_{\text{LCP}} E_{\text{in}} \tag{6}$$

$$\begin{pmatrix} E_{x,\text{out}} \\ E_{y,\text{out}} \end{pmatrix} = \begin{pmatrix} \cos^2(2\theta) & \cos(\theta)\sin(\theta) \\ \cos(\theta)\sin(\theta) & \sin^2(2\theta) \end{pmatrix} \begin{pmatrix} \cos\left(\frac{\delta}{2}\right) + i\sin\left(\frac{\delta}{2}\right)\cos(2\phi) & i\sin\left(\frac{\delta}{2}\right)\sin(2\phi) \\ i\sin\left(\frac{\delta}{2}\right)\sin(2\phi) & \cos\left(\frac{\delta}{2}\right) - i\sin\left(\frac{\delta}{2}\right)\cos(2\phi) \end{pmatrix} \begin{pmatrix} \frac{1}{2} & \frac{-i}{2} \\ \frac{i}{2} & \frac{1}{2} \end{pmatrix} \begin{pmatrix} E_{x,\text{in}} \\ E_{y,\text{in}} \end{pmatrix} \tag{7}$$

The angle θ corresponds to the orientation of the linear polarizer, δ is the sample retardance, ϕ is the sample slow axis orientation., and $i = \sqrt{-1}$. The retardance slow axis relates to the orientation of light that passes through the largest index of refraction in a birefringent material. Note that E_{in} is arbitrary, as the circular polarizer first converts light to linearly polarized along one direction regardless of the polarization state of the incident light, before then sending it through the quarter wave plate. For the sake of consistency, we will use an E_{in} of $\begin{pmatrix} 1 \\ 0 \end{pmatrix}$. There are four separate ray paths to consider for these calculations to determine the retardance magnitude and orientation experienced by light entering a single camera pixel corresponding to the 4 separate linear polarizer orientations. These orientations are either 0°, 45°, 90°, or 135°, resulting in four unique output Jones vectors as shown in equations 8 through 11. Note that similar mathematical analysis is performed by Bai et al.[14] for their DoFP polarimeter configuration, and that much of this mathematical analysis is derived from that setup.

$$\begin{pmatrix} E_{x,0^\circ} \\ E_{y,0^\circ} \end{pmatrix} = \begin{pmatrix} \frac{1}{2}\left(\cos\left(\frac{\delta}{2}\right) + \mathrm{i}\sin\left(\frac{\delta}{2}\right)\cos(2\phi) - \sin\left(\frac{\delta}{2}\right)\sin(2\phi)\right) \\ 0 \end{pmatrix} \tag{8}$$

$$\begin{pmatrix} E_{x,45^\circ} \\ E_{y,45^\circ} \end{pmatrix} = \begin{pmatrix} \left(\frac{1}{4} + \frac{i}{4}\right)\left(\cos\left(\frac{\delta}{2}\right) + \sin\left(\frac{\delta}{2}\right)\cos(2\phi) + \mathrm{i}\sin\left(\frac{\delta}{2}\right)\sin(2\phi)\right) \\ \left(\frac{1}{4} + \frac{i}{4}\right)\left(\cos\left(\frac{\delta}{2}\right) + \sin\left(\frac{\delta}{2}\right)\cos(2\phi) + \mathrm{i}\sin\left(\frac{\delta}{2}\right)\sin(2\phi)\right) \end{pmatrix} \tag{9}$$

$$\begin{pmatrix} E_{x,90^\circ} \\ E_{y,90^\circ} \end{pmatrix} = \begin{pmatrix} 0 \\ \frac{1}{2}\left(\mathrm{i}\cos\left(\frac{\delta}{2}\right) + \sin\left(\frac{\delta}{2}\right)\cos(2\phi) + \mathrm{i}\sin\left(\frac{\delta}{2}\right)\sin(2\phi)\right) \end{pmatrix} \tag{10}$$

$$\begin{pmatrix} E_{x,135^\circ} \\ E_{y,135^\circ} \end{pmatrix} = \begin{pmatrix} \left(\frac{1}{4} - \frac{i}{4}\right)\left(\cos\left(\frac{\delta}{2}\right) - \sin\left(\frac{\delta}{2}\right)\cos(2\phi) + \mathrm{i}\sin\left(\frac{\delta}{2}\right)\sin(2\phi)\right) \\ \left(\frac{1}{4} - \frac{i}{4}\right)\left(-\cos\left(\frac{\delta}{2}\right) + \sin\left(\frac{\delta}{2}\right)\cos(2\phi) - \mathrm{i}\sin\left(\frac{\delta}{2}\right)\sin(2\phi)\right) \end{pmatrix} \tag{11}$$

The camera detects and quantifies the intensity of light as opposed to the electric field amplitude. The relationship between the intensity of incident light and the electric field amplitude is given in equation 12:

$$I_{\text{out}} = |E_{\text{out}}|^2 = {E_{\text{out}}}^H * E_{\text{out}} \tag{12}$$

Here we define ${E_{\mathrm{out}}}^{H}$ as the complex conjugate of E_{out}. For each of the four linear polarizer orientations, the four separate output intensities are found to be:

$$I_{\mathrm{out},0} = \frac{1}{4} - \frac{1}{2}\cos\left(\frac{\delta}{2}\right)\sin\left(\frac{\delta}{2}\right)\sin(2\phi) \tag{13}$$

$$I_{\mathrm{out},45} = \frac{1}{2}\cos\left(\frac{\delta}{2}\right)\sin\left(\frac{\delta}{2}\right)\cos(2\phi) + \frac{1}{4} \tag{14}$$

$$I_{\mathrm{out},90} = \frac{1}{2}\cos\left(\frac{\delta}{2}\right)\sin\left(\frac{\delta}{2}\right)\sin(2\phi) + \frac{1}{4} \tag{15}$$

$$I_{\mathrm{out},135} = \frac{1}{4} - \frac{1}{2}\cos\left(\frac{\delta}{2}\right)\sin\left(\frac{\delta}{2}\right)\cos(2\phi) \tag{16}$$

Using the contrast relationship between orthogonal polarization orientation intensities, two additional variables can be defined to relate equations 13 through 16 to each other:

$$A = \frac{I_{\mathrm{out},90} - I_{\mathrm{out},0}}{I_{\mathrm{out},90} + I_{\mathrm{out},0}} = 2\cos\left(\frac{\delta}{2}\right)\sin\left(\frac{\delta}{2}\right)\sin(2\phi) \tag{17}$$

$$B = \frac{I_{\mathrm{out},45} - I_{\mathrm{out},135}}{I_{\mathrm{out},45} + I_{\mathrm{out},135}} = 2\cos\left(\frac{\delta}{2}\right)\sin\left(\frac{\delta}{2}\right)\cos(2\phi) \tag{18}$$

Using these two variables, the measured retardance magnitude and slow axis orientation corresponding to the entire system including the sample of unknown retardance can be isolated as shown in equations 19 and 20. Note that these values correspond to a single pixel and are expressed here to denote spatial variance.

$$\delta(x,y) = \mathrm{asin}\left(\sqrt{A(x,y)^2 + B(x,y)^2}\right) \tag{19}$$

$$\phi(x,y) = \mathrm{atan2}\left(\frac{A(x,y)}{B(x,y)}\right) \tag{20}$$

Finally, the slow axis orientation is converted to a fast axis orientation for convenience as the fast axis orientation also directly corresponds to the axis relating to the difference in principal stresses at that location in the material.

$$\phi'(x,y) = \phi(x,y) + \frac{\pi}{2} \tag{21}$$

Performing these calculations for each detector pixel leads to the ability to rapidly create images of retardance magnitude and orientation in a transparent sample over the entire field of view of the objective used. Figure 10 shows a raw image of 8-bit intensity data from the camera without processing, while figure 11 shows the same image with false color representing retardance magnitude and fast axis orientation.

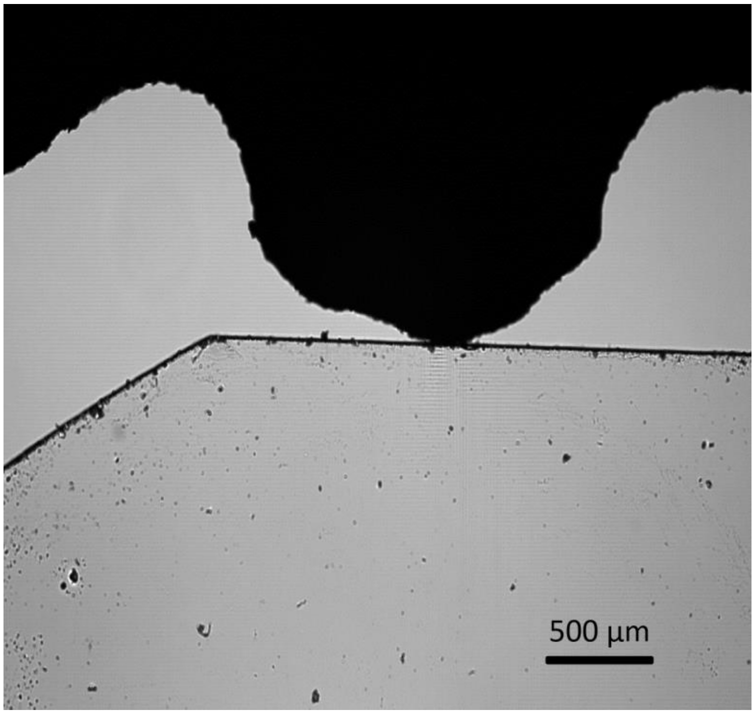

Figure 10: Raw image through a 5x objective to a Lucid Triton camera of a fused silica sample held in place by an aluminum contact point. The fused silica experiences a small amount of stress due to the external force of the contact. While the stress is not visible through raw imaging, the use of a DoFP detector does allow one to see a small amount of aliasing at the point of contact in the fused silica.

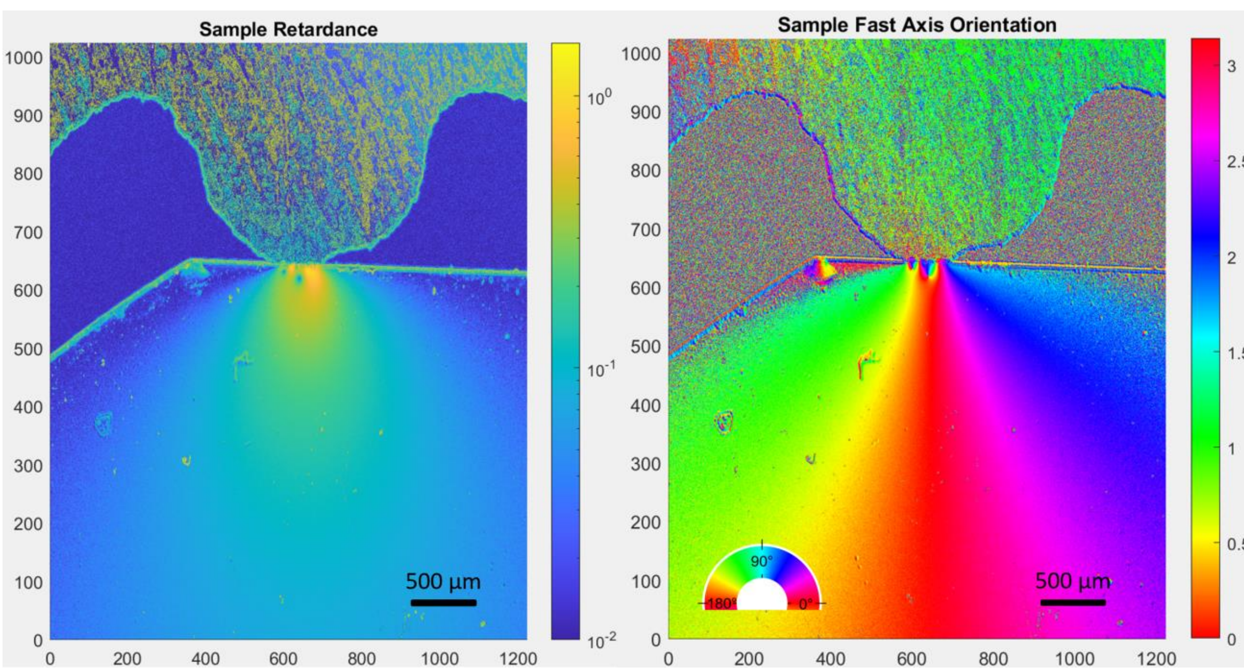

Figure 11: (Left) Intensity data from a raw image is processed to output retardance in radians at every super-pixel. The retardance is a direct function of birefringence, which is highest at the point of contact, and decreases as distance from the contact point increases. Color used to show magnitude in radians from 0 to π/2 on a logarithmic scale. (Right) Intensity data from figure 10 is processed to output fast axis orientation of the retardance at every super-pixel. Color is used to show fast axis orientation in radians from 0 to π.

Note that the retardance magnitude and orientation defined in equations 19 and 21 confine retardance magnitude to a 0 to $\frac{\pi}{2}$ radians range, and fast axis orientation to a 0 to π radians range. The retardance orientation is fully defined when constrained to a 0 to π radians range as orientation repeats every π radians. Therefore, an expected phase wrap-around will be present for a continuously changing retardance orientation that exceeds π or falls below 0. The retardance magnitude however can easily exceed $\frac{\pi}{2}$ radians for high birefringence materials such as many crystals and polymers[18]. This limits our proposed polarimetry technique to low birefringence measurements as high birefringence materials would result in a phase wrap-around for which we currently do not account. Specifically, we can use equation 1 to show that for a 0.5 mm thick fused silica sample observed with 632 nm light, the maximum measurable birefringence without potential phase wrap around is determined to be 6.32E-4. Such a value is greater than the expected maximum stress birefringence in fused silica due to laser-induced modifications, but there are many applications where this limit is far exceeded such as the quartz plate in figure 12, which exhibits birefringence higher than our maximum observable birefringence. Even with a thickness as low as 0.1 mm, our maximum measurable birefringence without potential phase wrap around is about 0.0032.

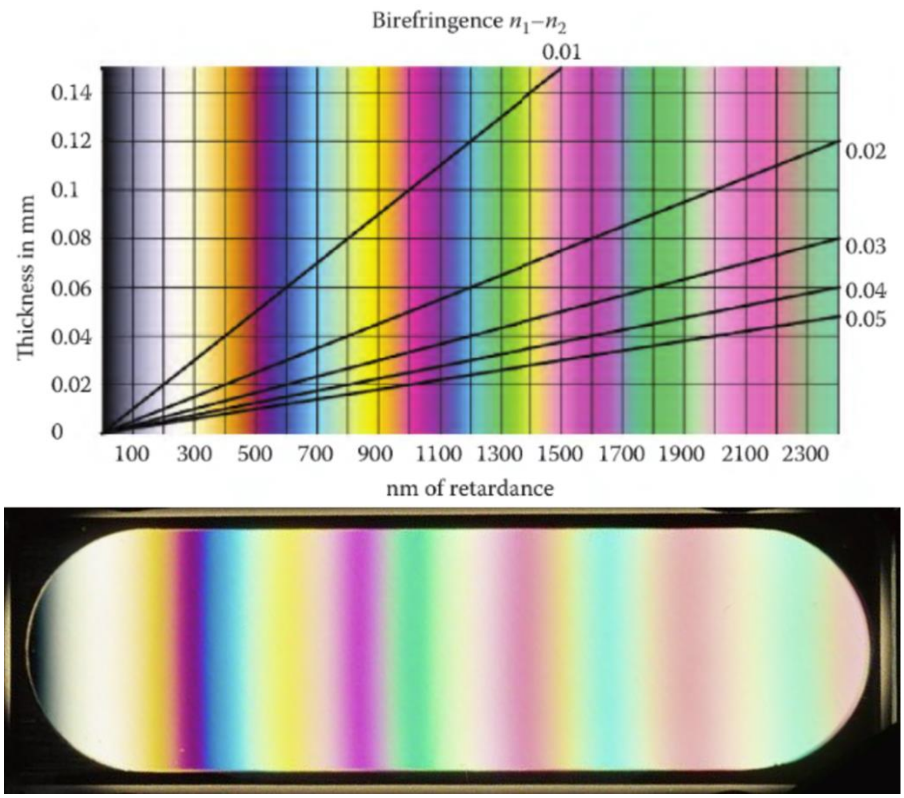

Figure 12: (Top) A Michael–Levy interference color chart used to categorize retardance and birefringence of a sample using color transmitted through a polariscope and sample thickness[19]. (Bottom) An illuminated variable thickness quartz wedge viewed through cross polarizers.

For the application of measuring stress birefringence from laser pulse induced modifications in fused silica, the phase wrapping issue is of little importance due to the relatively low magnitude of birefringence introduced. With these limitations in mind, there are still many necessary procedures to ensure result reproducibility. For example, measurements are always taken in the same ambient lighting, camera calibration conditions, and microscope illumination intensity. This ensures that the intensity of light that does not pass through any form of birefringence is the same for each imaging session. While unmodified fused silica should not have any intrinsic birefringence, images taken under these conditions still show as high as 0.025 radians of background retardance. This is due to the combination of many potential errors in the system, which will be further elaborated on in section 4.2. However, an estimation of the polarization effects due to any other component besides the measured sample can be calibrated out through a simple calibration technique[20]. As shown in equation 22, the Jones matrix of an object with arbitrary retardance is as follows:

$$J_b = \begin{pmatrix} \cos\left(\frac{\delta_b}{2}\right) + \mathrm{i}\sin\left(\frac{\delta_b}{2}\right)\cos(2\phi_b) & \mathrm{i}\sin\left(\frac{\delta_b}{2}\right)\sin(2\phi_b) \\ \mathrm{i}\sin\left(\frac{\delta_b}{2}\right)\sin(2\phi_b) & \cos\left(\frac{\delta_b}{2}\right) - \mathrm{i}\sin\left(\frac{\delta_b}{2}\right)\cos(2\phi_b) \end{pmatrix} \tag{22}$$

The background retardance measured with no sample present can be represented using the same Jones matrix. Furthermore, as we have determined that our polarimeter configuration is only sensitive to small retardances, we can use a paraxial approximation of δ such that $\sin\left(\frac{\delta}{2}\right) \approx \frac{\delta}{2}$ and $\cos\left(\frac{\delta}{2}\right) \approx 1$. This results in a simplified Jones matrix for an object of low arbitrary retardance:

$$J_b = \begin{pmatrix} 1 + \frac{i}{2}\delta_b\cos(2\phi_b) & \frac{i}{2}\delta_b\sin(2\phi_b) \\ \frac{i}{2}\delta_b\sin(2\phi_b) & 1 - \frac{i}{2}\delta_b\cos(2\phi_b) \end{pmatrix} \tag{23}$$

When a sample is introduced to the system with background retardance, a combined Jones matrix can be obtained as the following:

$$J_{\text{combined}} = J_b J_{\text{sample}} = \begin{pmatrix} 1 + \frac{i}{2}(\delta\cos(2\phi) + \delta_b\cos(2\phi_b)) & \frac{i}{2}(\delta\sin(2\phi) + \delta_b\sin(2\phi_b)) \\ \frac{i}{2}(\delta\sin(2\phi) + \delta_b\sin(2\phi_b)) & 1 - \frac{i}{2}(\delta\cos(2\phi) + \delta_b\cos(2\phi_b)) \end{pmatrix} \tag{24}$$

This combination of matrices can be represented as a single unknown matrix of low arbitrary retardance. Relating equation 23 to equation 24 leads to equations 25 and 26.

$$\delta_{\text{combined}}\cos(2\phi_{\text{combined}}) = \delta\cos(2\phi) + \delta_b\cos(2\phi_b) \tag{25}$$

$$\delta_{\text{combined}}\sin(2\phi_{\text{combined}}) = \delta\sin(2\phi) + \delta_b\sin(2\phi_b) \tag{26}$$

Experimentally, we are able to determine the retardance magnitude and orientation of just the background polarization effects, as well as that of the background effects combined with the sample. Therefore, we can solve for the retardance magnitude and orientation by rearranging equations 25 and 26 to isolate these variables. Furthermore, by applying the double angle formula to equations 17 and 18 and making the assumption that $\sin(\delta) \approx \delta$, we can make the following conclusions:

$$A \approx \delta\sin(2\phi) \tag{27}$$

$$B \approx \delta\cos(2\phi) \tag{28}$$

By applying this relationship to each term in equations 25 and 26, we find a simple calibration solution requiring only two images to be taken.

$$A = A_{\text{combined}} - A_b \tag{29}$$

$$B = B_{\text{combined}} - B_b \tag{30}$$

This means that as long as there is an image taken without the sample, as well as an image taken with a sample under the same environmental conditions, the retardance magnitude and orientation induced by just the sample itself can be determined. An example of the effects of calibration are shown in the following figures:

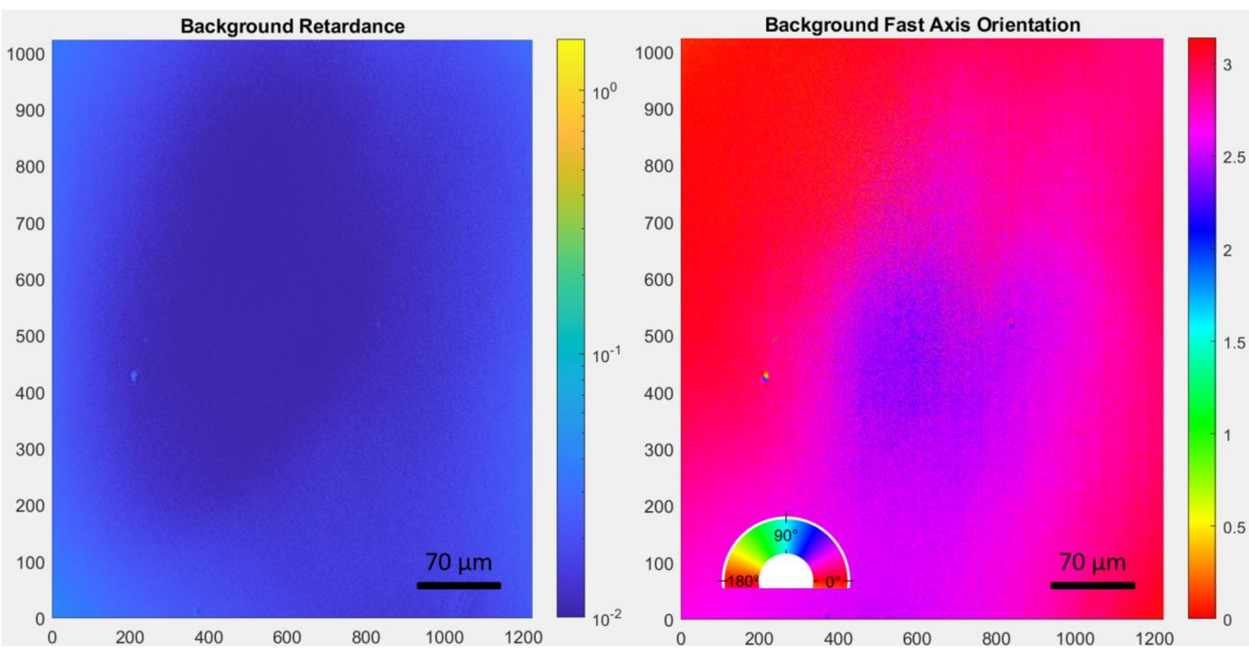

Figure 13: Background retardance magnitude and orientation in radians corresponding to fused silica with no modifications. Along with an overall background retardance magnitude profile, there is a spot corresponding to a defect in the circular polarizer, resulting in erroneous retardance calculation. Color values are in radians.

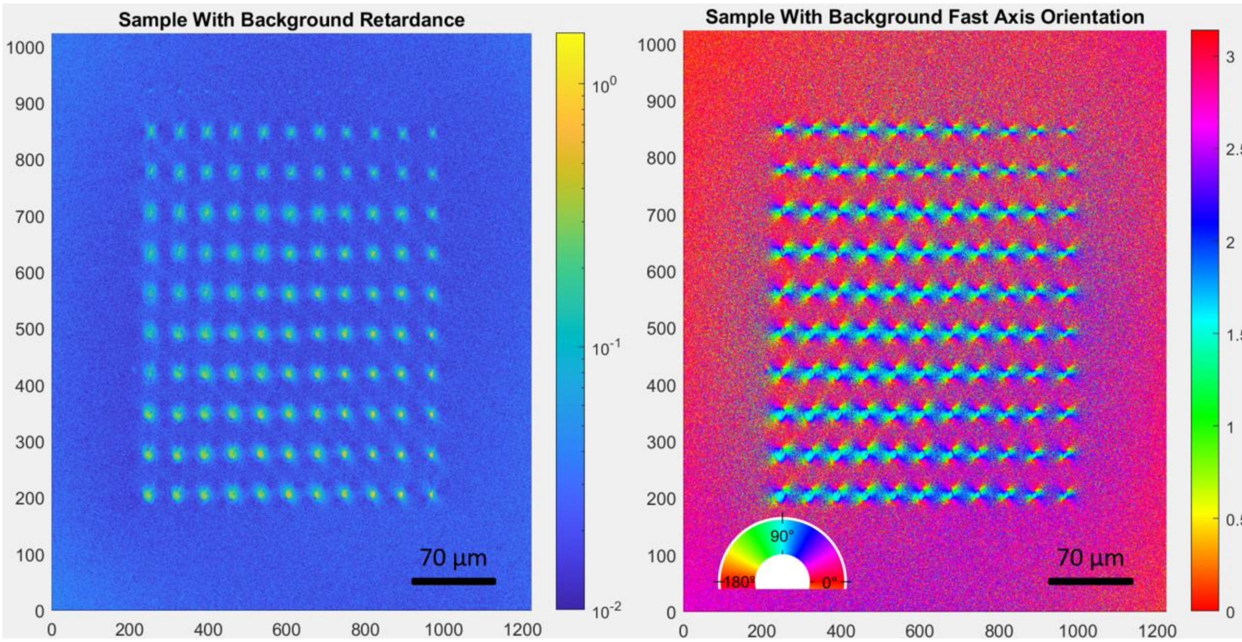

Figure 14: Retardance magnitude and orientation in radians corresponding to fused silica with a grid of modifications in it. The background has not yet been calibrated out. The modifications are a parameter scan of laser energy and pulse number. Laser energy decreases from left to right from 2820 nJ to 650 nJ, and pulse number increases from top to bottom from 1 to 200. Color values are in radians.

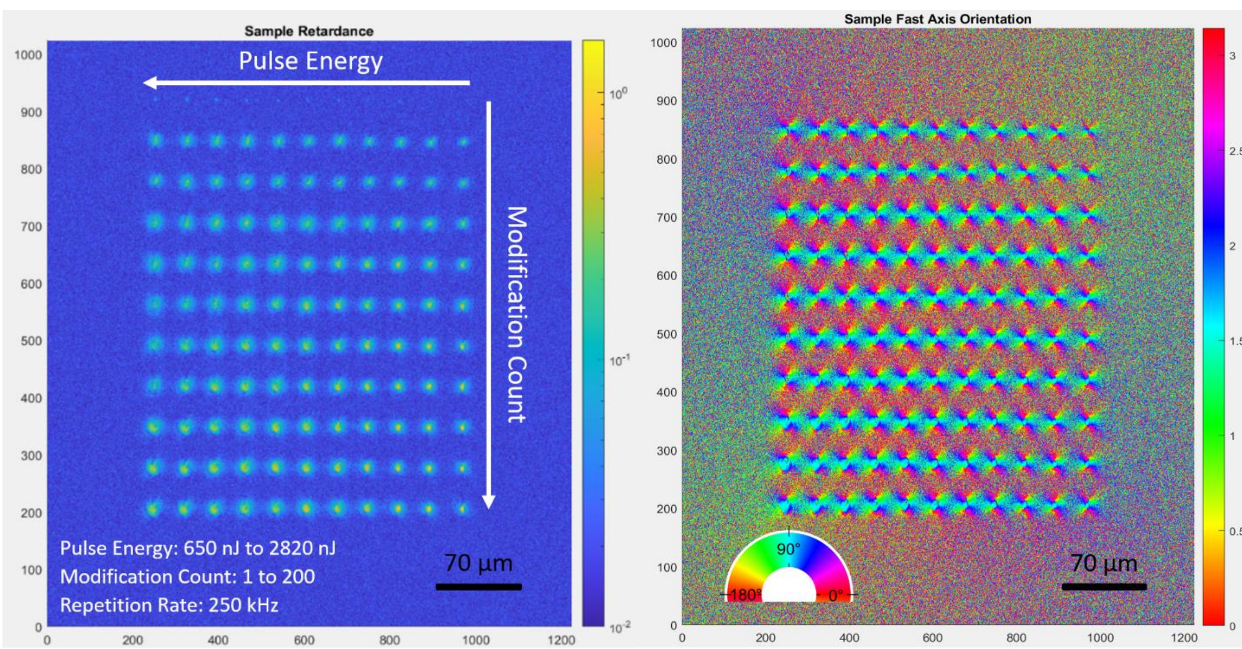

Figure 15: Calibrated image of modification grid. With the background removed, the retardance profiles become clearer. Most notably, the retardance orientation is much more apparent, and areas of negligible retardance magnitude leads to regions of noisy retardance orientation. Color values are in radians.

Note that due to background subtraction through calibration, the high retardance spot in figure 13 due to a defect in the circular polarizer is eliminated in the final calibrated image. While there is still some retardance magnitude noise in the final calibrated image, it is much less than what is originally present without use of the calibration technique.

2.3 Results Refinement

While single shot imaging allows for rapid birefringence characterization, this procedure is prone to sporadic fluctuations in intensity on each pixel due to various sources of noise. Fluctuation magnitude can reach as high as 8 intensity counts, which for an 8-bit detector, corresponds to an intensity uncertainty of about 3.1% at any given time. Such fluctuations happen over the course of fractions of a second, making it impossible to perfectly correlate calibration background images with images containing samples without accounting for this effect.

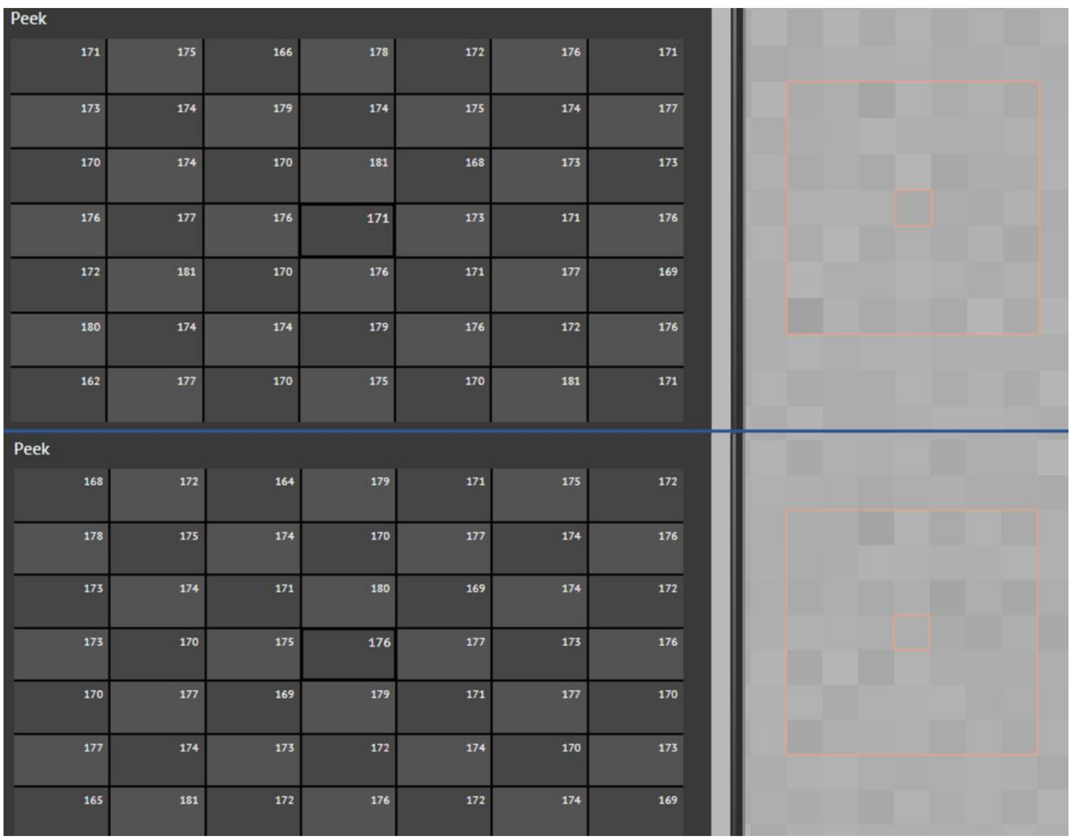

Figure 16: Sampled data from the Lucid Camera showing intensity values of an arbitrary grid of pixels. Top and bottom images are of identical pixel grids whose intensity values were recorded at two times separated by only a fraction of a second.

However, a simple and effective method to counteract this is to take multiple images and take an average over the range of intensities detected by a single pixel corresponding to one of four particular polarization orientations as shown in equation 31.

$$I(x,y) = \frac{1}{n}\sum_{i=1}^{n} I_i(x,y) \quad (31)$$

The averaged intensity values calculated for each polarization orientation at each location on the detector plane can then be used for retardance magnitude and orientation calculations. This procedure does make the assumption that the noise sources causing these fluctuations are centered around the true intensity value and are not skewed in any particular direction. Increasing the number of averaged images decreases background retardance magnitude and orientation noise in the results, as shown in figure 17.

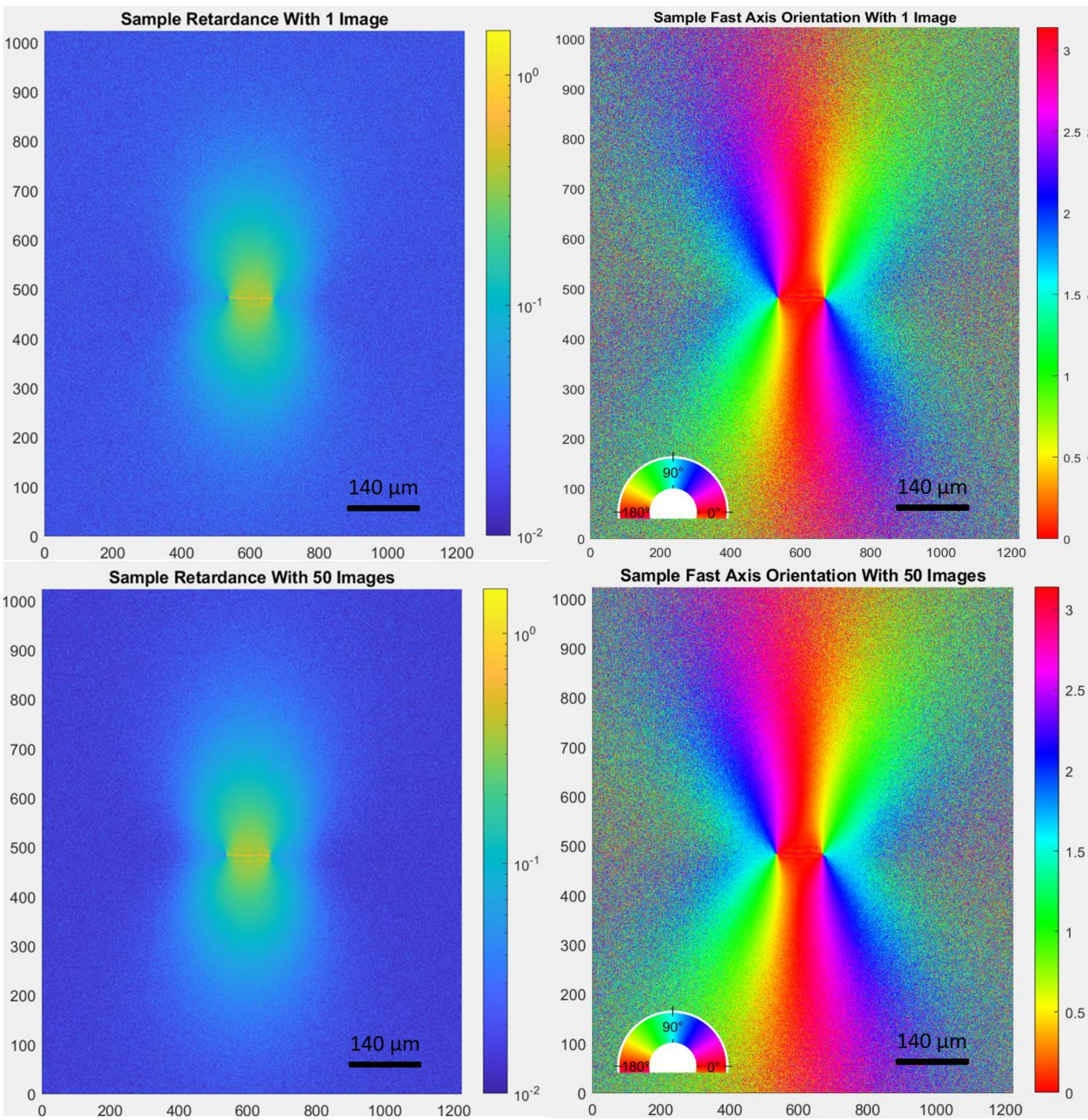

Figure 17: A comparison between taking a single image and averaging multiple images to produce retardance magnitude and orientation maps. Averaging multiple images improves background calibration, allowing for a clearer understanding of the retardance profile formed by the line of laser-induced modifications. Color values are in radians.

As the required exposure time for the camera is on the order of milliseconds, and the computational cost of processing multiple images is low, dozens of images can be taken without significantly increasing image processing time. As mentioned in section 2.1, another necessary method to improve the accuracy of the measured results is to decrease the NA of the illumination by decreasing the radial size of the aperture diaphragm. While each microscope is rated for a particular NA, the total NA can still be reduced at the expense of resolution. This decrease in resolution has an insignificant effect on the retardance magnitude and orientation measurements, as the stress fields surrounding the modifications are slow varying. As shown in figure 18, dropping the NA to as low as possible without overly reducing the light passing through the modification is key to improving result accuracy by eliminating artifacts due to rays experiencing a variety of optical paths before focusing to a single pixel.

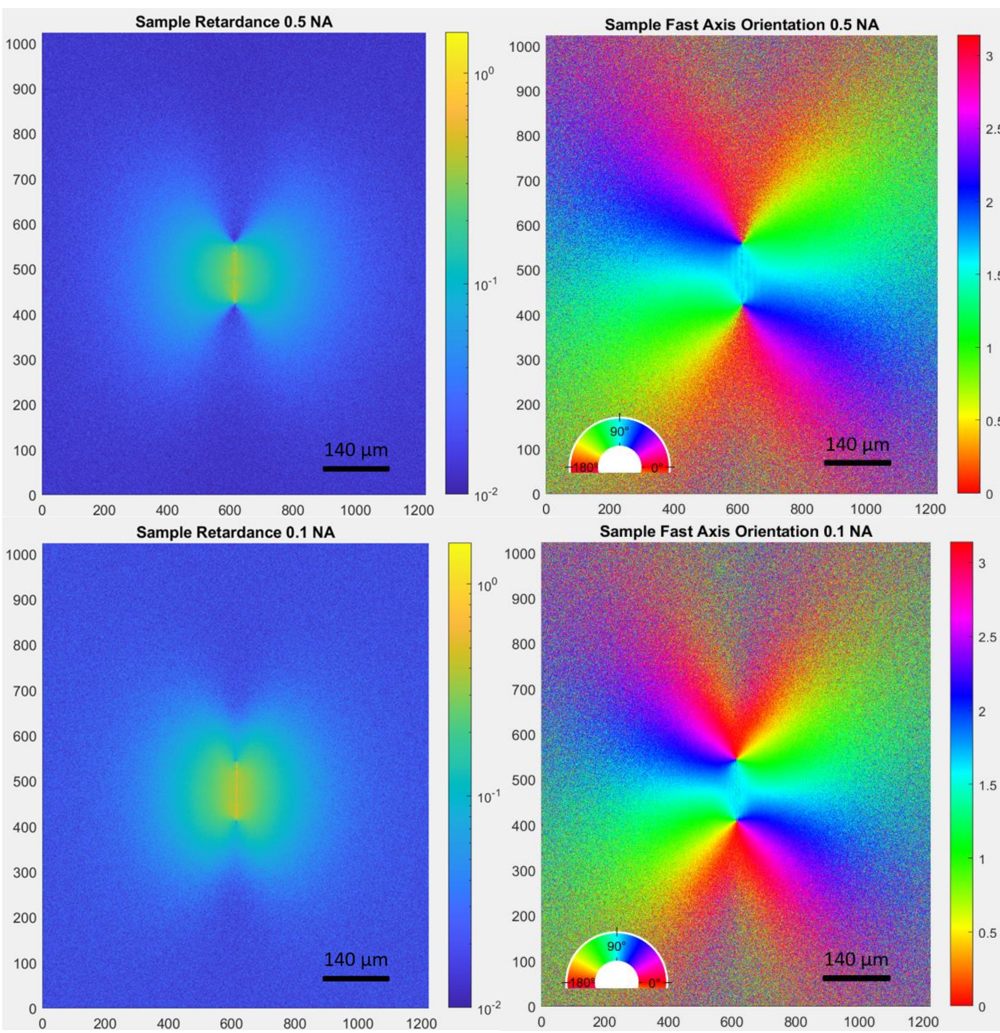

Figure 18: Comparison between results taken using 0.5 NA and results taken using 0.1 NA. At larger NA, there appears to be two nodes of low retardance at either end of the line of laser-induced modifications. This however is an artifact of the large NA, due to many rays passing through the modification and surrounding area at a wide variety of angles. Reducing the angle of acceptance from π/6 to π/31 largely reduces this error. Further convergence towards collimated light would reduce this error entirely. Color values are in radians.

2.4 Polarimeter in Reflection Mode

It is worth noting that many samples for which ULSF would be of value are used in reflective applications. As such, the original design for the BX-51 modification involved running the microscope in reflection mode. This significantly alters the Jones calculus used to determine retardance magnitude and orientation contributions from the observed sample. Not only would light experience a double pass through the sample itself before reflecting off the back surface, but the light would also pass through a non-polarizing plate beam splitter before and after interaction with the sample of interest. Such a configuration would require additional modeling of the Jones matrix of the polarization effects of the beam splitter itself in order to isolate the contributions of the observed sample. As the beam splitter is oriented at 45°, and likely consists of a thin metal coating for partial reflection, the Jones calculus involved would be significantly more complex as light reflecting from a smooth metal surface is affected by its complex refractive index[6]. Furthermore, a different Jones matrix would be required to account for the beam splitter when used in transmission and reflection. This would also require a more involved calibration technique to account for undesired effects both before and after the sample. Finally, such a configuration would result in non-uniform results for non-birefringent samples, as the circularly polarized light emitted by the left-hand circular polarizer would have a high magnitude of ellipticity as a result reflection off of, and transmission through the beam splitter. While a more robust retardance magnitude and orientation calculation procedure may be able to adequately account for these complexities, the transition to transmission-only measurements was deemed acceptable as results from experiments involving these samples will likely have a high correlation to results for samples of the same material with a reflective coating.

Chapter 3 – Finite Element Analysis

3.1 Modification Finite Element Model

Finite element analysis (FEA) is a widely used computational method utilized to solve complex behavior due to a large variety of loading types. At a high level, FEA involves dividing a complex physical system into small, interconnected finite elements. In the case of a static structural FEA, the solution is approximated to partial differential equations that describe the static force equilibrium of a continuous body. That continuous body is broken up into discrete nodes, whose displacements are used to calculate stress and strain. Such an analysis can be used to form an estimated model of the stresses produced by a laser-induced modification in fused silica. For our application, the FEA tool ANSYS Parametric Design Language (APDL) was used due to its versatility and script driven behavior. In order to model the fused silica, a variety of material properties are required. These are the elastic modulus, Poisson's ratio, shear modulus, and coefficient of thermal expansion of fused silica. It is important to note that while these values are all generally tensors, as fused silica is an isotropic material, a single value can be defined for each. The elastic modulus or Young's modulus (E) of a material describes a stiffness property of the material and is defined by the ratio of stress applied to the strain produced in the material. For an isotropic material like fused silica,

$$E = \frac{\sigma_{xx}}{\epsilon_{xx}} \tag{32}$$

The Poisson's ratio (ν) is a dimensionless property that describes the relationship between the deformation of a material along one particular direction and its deformation perpendicular to that direction. This value is required to calculate the deformation of a material under loading.

$$\nu = -\frac{\epsilon_{\mathrm{xx}}}{\epsilon_{\mathrm{yy}}} \tag{33}$$

Similar to elastic modulus, the shear modulus (G) is defined as the ratio of the shear stress to the resulting shear strain in the material. For an isotropic material,

$$G = \frac{\tau}{\gamma} = \frac{E}{2(1+\nu)} \tag{34}$$

Finally, the coefficient of thermal expansion (α) is the amount of expansion or contraction that a material undergoes when subjected to changes in temperature.

$$\alpha = \frac{1}{L}\frac{\delta \mathrm{L}}{\delta \mathrm{T}} \tag{35}$$

In this case, L refers to any dimension of the material subject to thermal change. Many sources provide material properties of fused silica, and each provides slightly different ranges of values. For this analysis, the chosen values for elastic modulus, Poisson's ratio, shear modulus, and coefficient of thermal expansion of fused silica are 72 GPa, 0.17, 30.77 GPa, and 0.5 ppm/K[21,22] respectively. Note that the value for the coefficient of thermal expansion is a relatively arbitrary choice, as the actual thermal load caused by ultrafast laser pulses will not be modeled directly, as will be touched on further in this section. With these material properties defined, the resulting stresses in a material due to a thermal load can be determined. However, in order to output these stresses, the laser-induced modification model needs to be fully defined and constrained. For finite element analysis, it is important to decide the way nodes and elements are defined to provide an accurate representation of the physical model and its interaction with various loads. In APDL, the element type SOLID187 is used for modeling the laser-induced modification as this element type is a high-order 3D 10-node element, which interpolates the displacement solution with a piecewise-quadratic function, leading to a piecewise-linear stress field. This element type is displayed in figure 19.

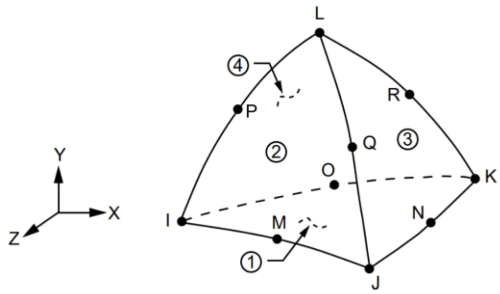

Figure 19: APDL SOLID187 tetrahedral element model with labeled nodes.

The laser-induced modification model requires a highly variable mesh to achieve high fidelity results by decreasing distance between nodes at high stress locations near the modification. With the element type defined, the actual geometry of the modification and surrounding material can be modeled. The modification itself is modeled as a cylinder which is 1 µm long, and 2 µm wide. In reality, laser-induced modifications are generally approximately ellipsoidal[5], but a cylindrical estimation is appropriate for preliminary modeling. The surrounding material is modeled as an arbitrarily large cylinder, such that the stresses at the model boundaries are orders of magnitude lower than those directly surrounding the modeled modification. The model is then meshed such that the modification and immediately surrounding volume consist of a high number of nodes. The node density then decreases with an increase in distance from the modification to improve computational efficiency as stresses further from the modification are significantly lower than those near it. Figure 20 provides a visualization of the model and mesh.

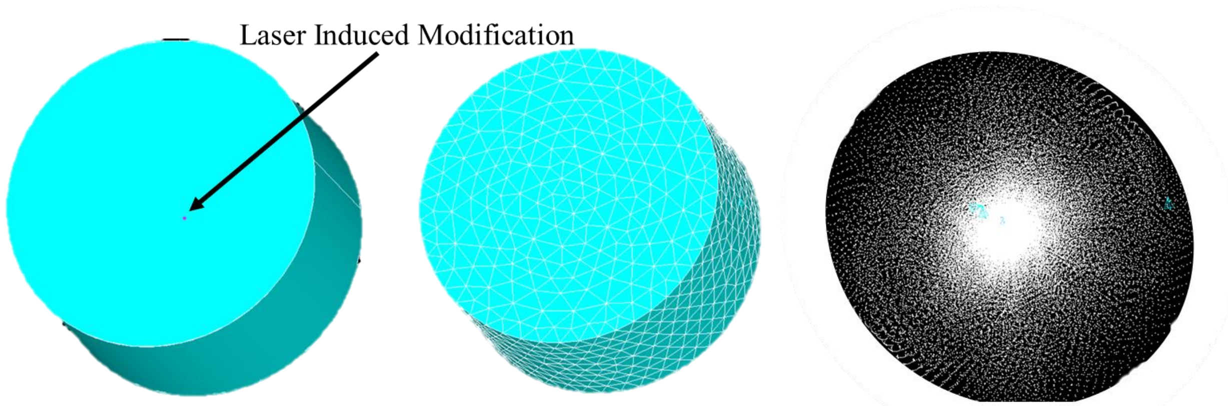

Figure 20: (Left) Model of laser-induced modification with surrounding material. (Middle) Meshed model. (Right) View of only the nodes generated from meshing. The node density near the center of the volume is significantly larger than that towards the edges of the material.

With the geometric modeling complete, a thermal load can be applied to simulate the stresses experienced by the material in the modification region due to the laser pulses. While there are stresses in the material due to thermal expansion, the thermal load applied here is to simulate the general stress profile in the modification and surrounding material due to modification generation. In other words, the temperature applied in the finite element analysis is not meant to directly simulate thermal expansion, but rather the total stress profile induced in the substrate. The actual temperature load magnitude caused by the laser pulses will vary with pulse energy and pulse rate and is not numerically accounted for in this simulation. While this is the only load of significance for stress generation, displacement loads must also be placed on the model to ensure it is fully constrained. A kinematic coupling is ideal in this scenario to allow the modification to freely expand due to the thermal load, without being under-constrained. To achieve this, 3 displacement loads are placed on 3 separate nodes. One node at the center of the modification is constrained in x, y, and z displacement. This limits the model from translating around in space. Another displacement load was placed along the z-axis at a node at the top of the model, which constrained x and y rotation. At this point, the model can expand from the center, and rotate about the z-axis. A final displacement load was placed at a node on the edge of the sample along the x-axis, constraining motion only along the y direction. As such, the model cannot experience any rigid body motions, but will be able to freely expand from the center of the model due to the thermal load. With all loading in place, the stresses in the modification and surrounding material can be solved at each node. Cross-sectional data of the Von Mises stress in the modification is shown in figure 21.

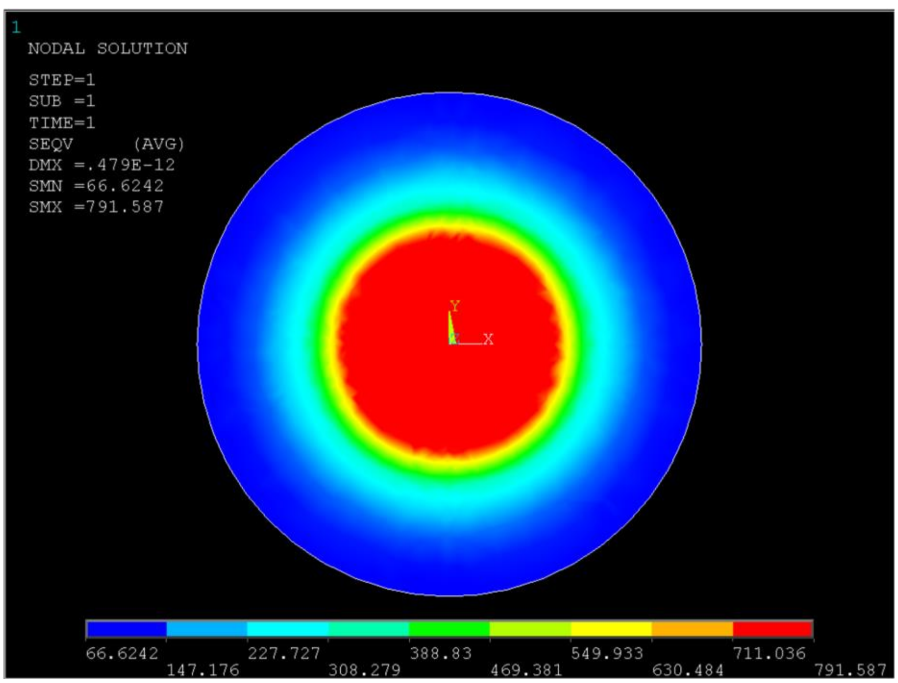

Figure 21: Von Mises stress results of a central cross section of the laser-induced modification and surrounding material FEA model. As a temperature load on fused silica causes expansion in all dimensions, results are axially symmetric about the z-axis.

Note that units are not given in the FEA results, as they must be tracked separately, requiring much care when defining material properties, and interpreting solution results. While Von Mises stress results are helpful for viewing equivalent stresses in a material, the output results of interest are the stresses along the x, y, and xy directions (these are σ_x, σ_y, and τ_{xy}). This is because this simulation is designed for stress birefringence measurement along the z-axis. Therefore, any stresses along the z axis will not cause birefringence in the direction of propagation. Such a statement is valid, as we are assuming the NA in the imaging polarimeter is low enough that light rays are approximately collimated along the z-axis. Therefore, birefringence measurements made by the imaging polarimeter should in theory match with results from this simulation for modifications of the same parameters. Stress birefringence is a function of the material stress-optic coefficient and the difference in principal stresses as shown in equation 36:

$$\Delta \mathrm{n} = C(\sigma_1 - \sigma_2) \tag{36}$$

Note that the stress optic (or photo-elastic) coefficient (C) is a material property that describes the relationship between stress and the resulting change in the refractive index of a material:

$$C = \frac{1}{n}\frac{\delta \mathrm{n}}{\delta \sigma} \tag{37}$$

As with other material properties, the value for the stress-optic coefficient of fused silica varies from a number of sources. However, a value of 2.43E-12 1/Pa was chosen for this analysis based on an extensive study done by NASA Langley Research Center[23]. Using the σ_x, σ_y, and τ_{xy} outputs at each node from the FEA of the laser-induced modification, the difference in principal stresses and their orientations throughout the model can be determined through the use of Mohr's circle.

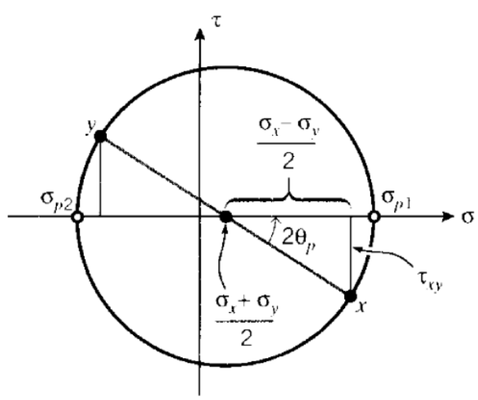

Figure 22: Mohr's circle with relevant parameters for determining principal stresses and their orientation using x, y, and shear stresses[24].

This application of Mohr's circle shows that the values of the principal stresses are:

$$\sigma_{\mathrm{p1}} = \frac{\sigma_x + \sigma_y}{2} + \sqrt{(\frac{\sigma_x - \sigma_y}{2})^2 + \tau_{\mathrm{xy}}{}^2} \tag{38}$$

$$\sigma_{\mathrm{p2}} = \frac{\sigma_x + \sigma_y}{2} - \sqrt{(\frac{\sigma_x - \sigma_y}{2})^2 + \tau_{\mathrm{xy}}{}^2} \tag{39}$$

Therefore, the difference between them is:

$$\sigma_{\mathrm{p1}} - \sigma_{\mathrm{p2}} = 2\sqrt{(\frac{\sigma_x - \sigma_y}{2})^2 + \tau_{\mathrm{xy}}{}^2} \tag{40}$$

Finally, we see that the angle between them is:

$$\theta_p = \frac{1}{2}\mathrm{atan}\left(\frac{2\tau_{\mathrm{xy}}}{\sigma_x - \sigma_y}\right) \tag{41}$$

Experimentally, retardance magnitude and orientation are given as results. In order to relate simulated results to experimental results, we can relate equation 1 to equation 36 to get the relationship between the difference in principal stresses and retardance magnitude:

$$\delta = \frac{2\pi}{\lambda} C(\sigma_1 - \sigma_2) * t \tag{42}$$

Furthermore, the fast axis of retardance is equivalent to the angle θ_p calculated in equation 41. Therefore, we can output the same type of results for both the experimental and finite element data if we can ray trace through the simulated results and calculate the retardance orientation and magnitude experienced by each ray.

3.2 Retardance Magnitude and Orientation Calculation

Nodal coordinate data and the outputs for σ_x, σ_y, and τ_{xy} at each node can be exported into MATLAB to complete data processing and simulate tracing "rays" through the material. As we can assume rays are collimated through the sample along the z-axis, we must account for all retardance contributions due to the stress birefringence throughout the sample. To accurately estimate these retardance contributions, the sample is divided into many sections that each have a constant retardance magnitude and orientation, as well as a finite thickness. Although over 280,000 nodes with stress results were generated, the chances of an individual ray passing through the exact location of each node in each divided section is close to none. However, due to the nature of stress propagation in a material, this can be accounted for by linearly interpolating stress results from the closest three nodes and applying that as the stress experienced by the ray at that particular material section. Interpolation also allows us to convert the highly variable mesh to a uniform mesh with sections of constant thickness as shown in figure 23.

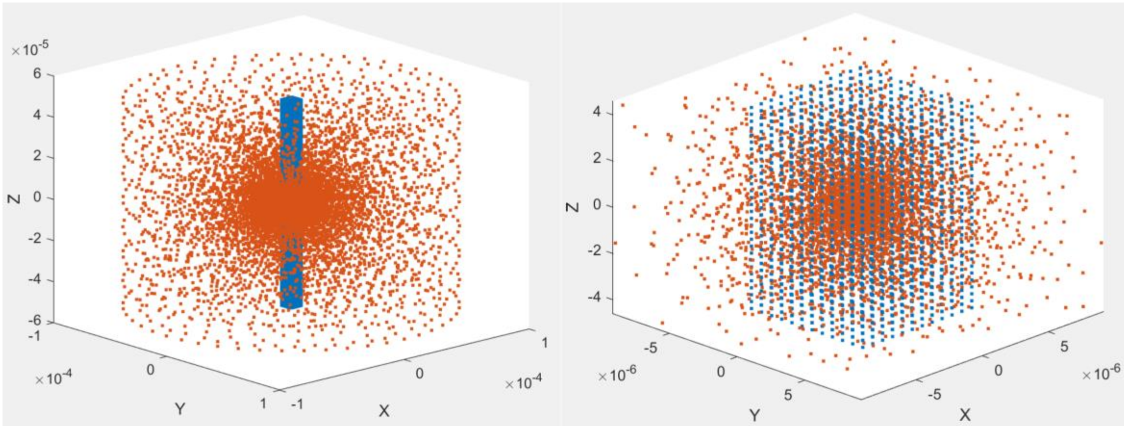

Figure 23: (Left) Original nodal coordinate data from FEA in orange, with uniform interpolated coordinate data in blue. (Right) Zoomed view of the center of the sample to better demonstrate nodal uniformity.

Doing this for each stress type, at each divided section, allows us to add up the total σ_x, σ_y, and τ_{xy} stresses experienced by each ray. We then are able to use equations 40, 41, and 42 to output the retardance magnitude and orientation experienced by each ray. Figure 24 shows the output for the FEA results with the input parameters described throughout this section.

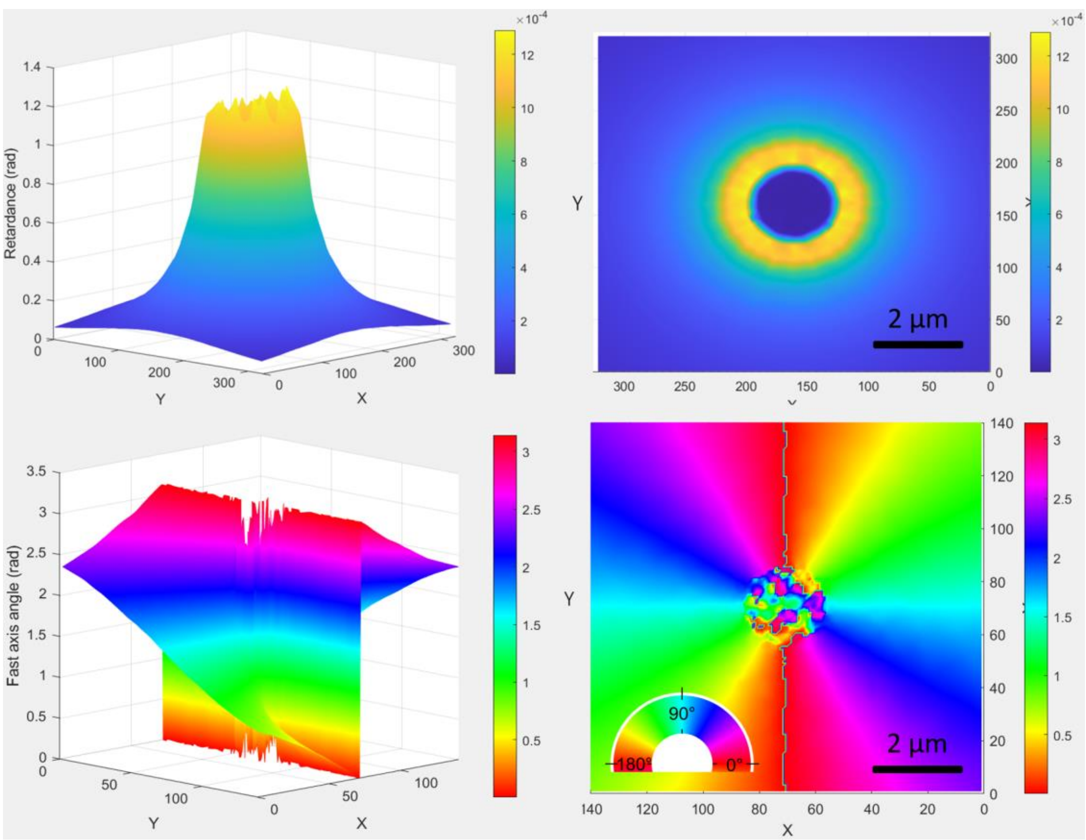

Figure 24: (Top) Orthogonal and top-down retardance magnitude results from FEA data of the central region of the sample. (Bottom) Orthogonal and top-down retardance orientation results from FEA data of the same sample region. Color values are in radians.

A number of qualitative observations can be drawn from these results. First, due to the positive thermal load induced in modification, the orientation of the resulting retardance in the surrounding material remains parallel to the modification edge at all locations. This is because the modification is compressing the surrounding material due to thermal expansion. As such, the compressive direction of stress is perpendicular to the modification edge, and the tensile direction is parallel to the modification edge. The refractive index is lower along the tensile direction, which corresponds to the fast axis of retardance, which is the orientation at which light passes through the material the fastest. Although figure 17 consists of multiple single modifications in a line, a similar retardance orientation profile is visible. Inside the modification itself, the orientation of retardance is noisy and uncertain. This is because the magnitude of retardance in the modification is 0 regardless of the magnitude of the thermal load applied. This is because the modification has been modeled as an isotropic material experiencing an equibiaxial stress, meaning it experiences the same magnitude of stress in all directions. Therefore, no retardance can be generated as no phase difference will be produced regardless of polarization orientation. However, retardance just outside the modification spikes due to the large compressive stresses experienced by the surrounding material. Interestingly, using the aforementioned material properties and load parameters, the extent of significant retardance along a particular direction in fused silica appears to only be about 1 – 2 μm. Furthermore, the maximum magnitude of retardance under these conditions is only about 0.0012 rad, which corresponds to about 0.12 nm of retardance for 632 nm light. While the retardance from a single modification is relatively low, in the case of ULSF, many overlapping laser-induced modifications are generated during the figuring process, resulting in compounding retardances with similar if not equal orientations. However, in order to compare the finite element model results with experimental results, single "dot" modifications were made for observation with the constructed imaging polarimeter. This is further explored in section 4.1.

3.3 Accounting for Non-Equibiaxial Stresses

The finite element model described thus far incorporates an isotropic laser-induced modification, whose coefficient of thermal expansion is the same in all directions. While fused silica is an isotropic material, the laser used to generate the modifications is polarized. This causes the formation of non-equibiaxial stress surrounding the material depending on the polarization orientation of the laser[25], which will have an effect on the measured stress birefringence. While modeling laser polarization is not possible in a static structural FEA, one way to account for the non-equibiaxial stress produced is to adjust the simulated coefficients of thermal expansion of the modification itself. As the simulated thermal load is applied as a means of generating an expected stress profile, the ratio between the material CTE_x and CTE_y of the modification region can be adjusted to generate stresses inside the modification during thermal expansion due to material anisotropy. This will also produce a non-axially symmetric stress profile surrounding the modification. Figure 25 shows the Von Mises stresses in a cross section of the finite element model with an anisotropic modification.

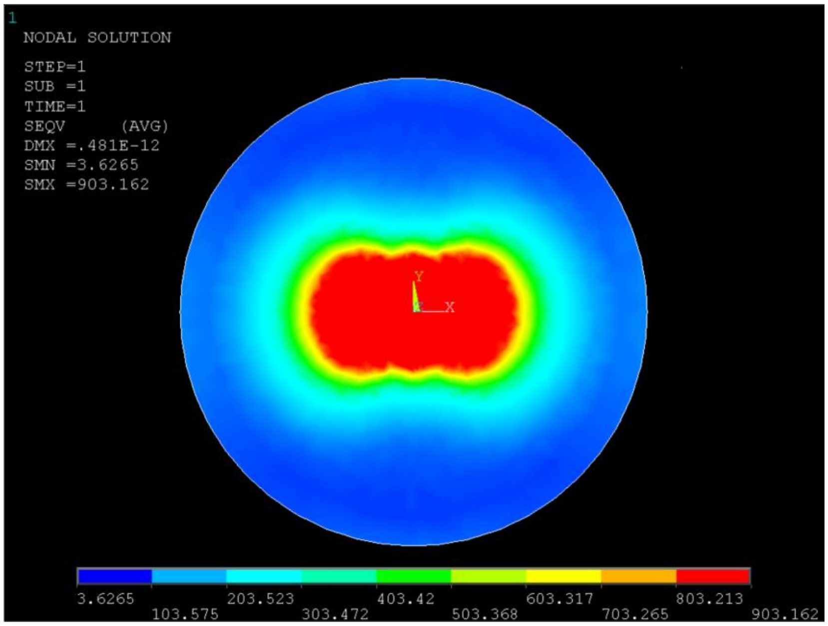

Figure 25: Von Mises stress results of a central cross section of the laser-induced modification with a CTE_x to CTE_y ratio of 10. Note the asymmetry of the equivalent stress results due to the ratio between perpendicular coefficients of thermal expansion.

This artificial modeling of the effects of laser polarization may help us understand the stress contributions of the laser polarization orientation during modification formation. Interestingly, the stress-induced birefringence inside the modification is non-zero for a CTE_x to CTE_y ratio other than 1. Figure 26 shows the retardance magnitude and orientation results from the analysis results in figure 25.

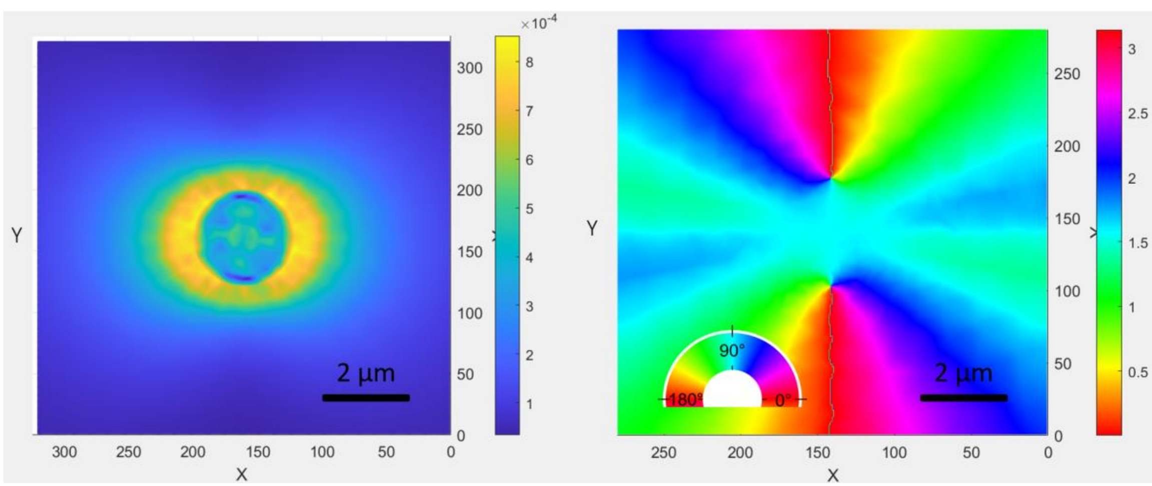

Figure 26: (Left) Retardance magnitude results from anisotropic CTE FEA data of the central region of the sample. The magnitude of retardance asymmetry is correlated with the ratio between CTE_x and CTE_y. (Right) Retardance orientation results from FEA data of the same sample region. Color values are in radians.

The ratio between the material CTE_x and CTE_y can be adjusted in an attempt to match the results produced experimentally. This is possible as this ratio has a significant impact on the magnitude of the retardance in the modification as well as the extent of asymmetry of the surrounding retardance magnitude and orientation. If a correlation between the experimentally formed stress fields with nanogratings and the stress results from the FEA of the anisotropic modification can be made, then the simulation results can be used to differentiate between the stresses due to the general formation of the modification, and the non-equibiaxial stresses produced due to laser polarization. The simulation may also then be useful to categorize the form birefringence caused by the nanogratings produced inside the modification itself.

Chapter 4 – Experimental Output and Uncertainty

4.1 Retardance Magnitude and Orientation of Single Modifications

With the polarimeter configuration fully defined, the data extraction and calibration technique in place, and a finite element model established for a single modification, retardance magnitude and orientation results of single modifications can be explored in order to relate finite element results to experimental data. Figure 15 above is an image of a grid of single “dot” modifications corresponding to various laser pulse energies (from 650 nJ to 2820 nJ) along one axis and number of pulses (from 1 to 200) in each dot along the other. Each modification was made using a laser pulse repetition rate of 250 kHz. The modifications were made using a wide variety of parameters as the exact total expected retardance produced by these single modifications was still unknown. By fitting all of these modifications into a single field of view, their relative retardance due to stress birefringence can quickly be qualitatively characterized before each modification is viewed individually. As the effects of increasing pulse number in a single modification are not yet well characterized, it would be best to view the retardance magnitude and orientation of a modification made with a single laser pulse. However, the magnitude of retardance of a single pulse laser-induced modification is too weak compared to the background noise in the imaging polarimeter even with background calibration. As shown in figure 27, even the creation of a modification made by 20 stationary lasers pulses results in a small retardance profile.

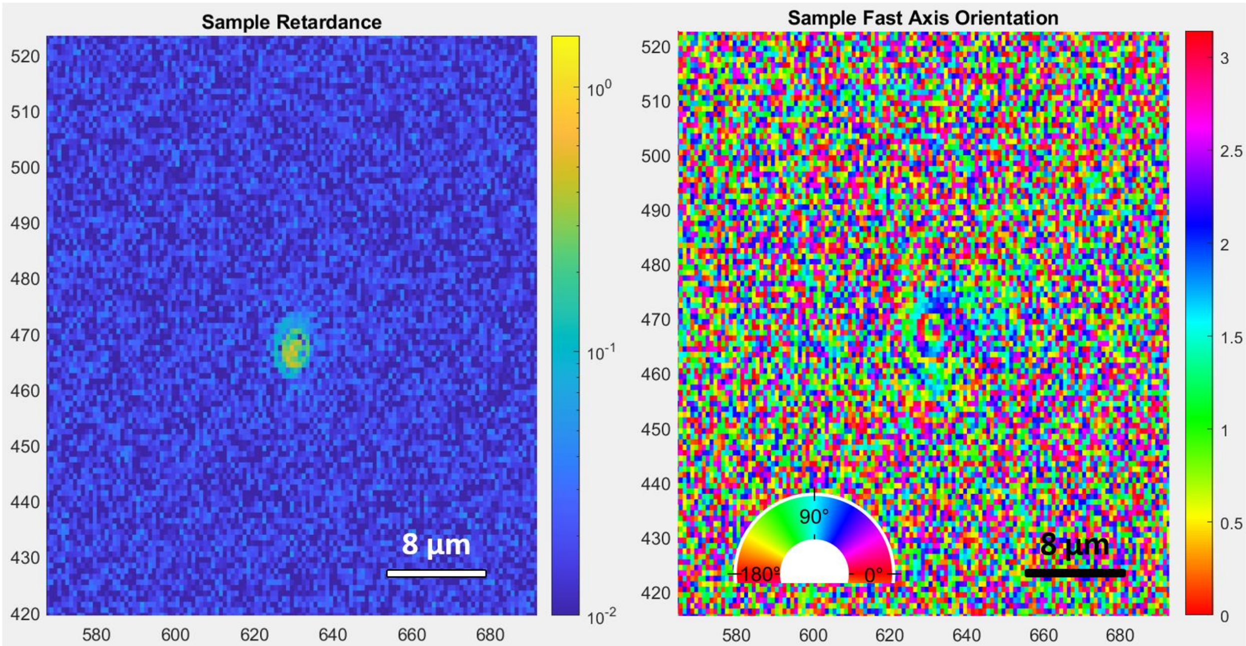

Figure 27: (Left) Retardance magnitude of a single modification made at 980 kHz, 2820 nJ, and 20 laser pulses. (Right) Fast axis orientation of the modification and background. Color values are in radians.

Furthermore, the modification itself is almost too small to resolve using a 40x objective, which is the highest magnification available to us using our current configuration of the BX-51 microscope. At this magnification, the extent of the modification itself is only about 4 to 5 pixels wide, while the extent of the retardance field is about twice that amount. While there is resolvable retardance surrounding the modification, it is likely that this is due to more effects than just stress birefringence or form birefringence caused by nanogratings. If the FEA results are accurate, and we assume that the birefringence of overlapping laser pulses adds linearly, then we would expect the maximum approximate retardance of the stress field surrounding the modification to be about 20 times the maximum retardance recorded in figure 24. This would result in a retardance of 0.024 radians, or about 2.4 nm for 632 nm light. While this is resolvable using our imaging polarimeter, it is much lower than the maximum recorded retardance shown in figure 27. The existence of erroneous retardance results is clear when viewing results for 200 laser pulses, as shown in figure 28.

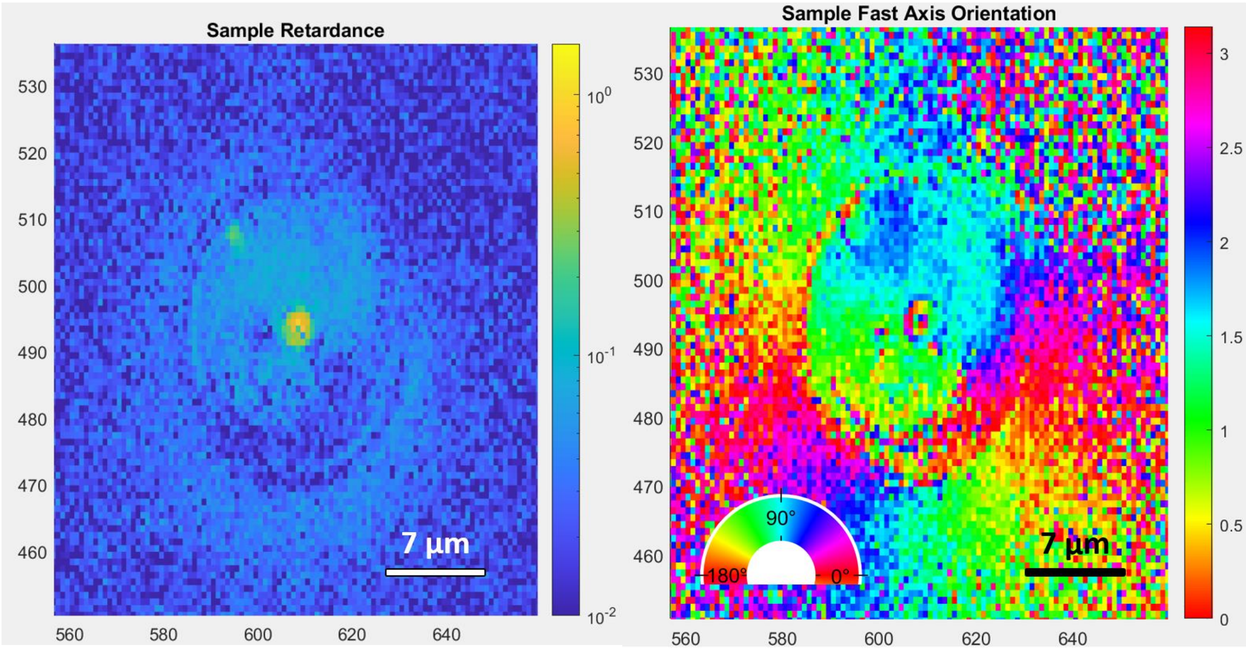

Figure 28: Retardance magnitude of a single modification made at 980 kHz, 2820 nJ, and 200 laser pulses. (Right) Fast axis orientation of the modification and background. Color values are in radians.

While the measured retardance increased with an increase in the number of laser pulses in a single modification, more important observations can be made regarding the stress field irregularity. The retardance magnitude data shows multiple areas of high and low retardance that are not symmetric around the central modification region. Furthermore, the fast axis orientation data highlights a few more areas contributing to the retardance that are outside the stress region. Images taken while focusing through the modification give light to these undesired sources of retardance as shown in figure 29.

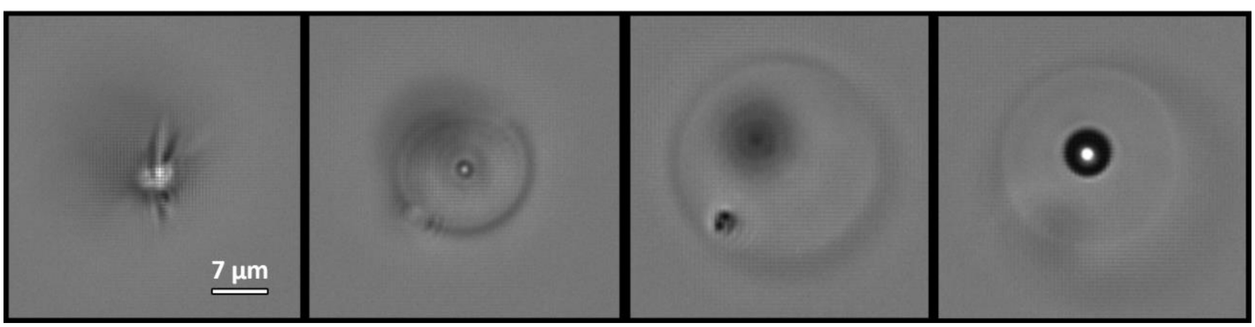

Figure 29: Intensity images of multiple artifacts produced when a single modification is made at 980 kHz, 2820 nJ, and 200 laser pulses. Images taken through a 40x objective through focus over a depth of 20 µm.

These images represent a variety of artifacts produced when a single laser-induced modification was made. These images were taken over a depth of about 20 µm and reveal the many other contributors to the overall sample retardance. The first image appears to be a localized fracture due to failure of the fused silica from overlapping laser pulses. The second image is likely the actual modification itself, the third image shows an unknown artifact, and the final image is likely that of a bubble formed in the process of rapid heating and cooling of the fused silica. Each of these contribute stresses of various magnitudes which entirely convolute the stress field produced by the modification itself. The formation of each of these effects is consistent for each of the modifications made in Figure 15 using the given parameters. This is true for modifications made using a pulse repetition rate of 980 kHz as well as 250 kHz. The only exception being the modifications made with only one laser pulse. However, higher magnification imaging is required to accurately resolve the modification itself. Furthermore, the retardance produced by the stress birefringence of a single pulse laser-induced modification is likely too low to reliably measure using the current imaging polarimeter configuration. Therefore, in order to quantitatively compare FEA results to experimental results, further improvements to the imaging polarimeter will need to be made.

4.2 Sources of Error and Potential Improvements

Due to the complexity of the imaging polarimeter, there are many sources of potential error and potential improvement. Each of these will be briefly explored, and where possible, uncertainty values will be estimated. One of the first uncertainties introduced to the system comes from the bandwidth filter used to limit light to being approximately monochromatic. As refractive index is a function of wavelength, an inherent refractive index uncertainty directly related to the bandwidth of the filter is present in our imaging polarimeter. Specifically, as the FWHM of the filter is 10 nm, the significant accepted bandwidth is from 622 nm to 642 nm, which corresponds to a refractive index range of 1.4573 to 1.4568 as shown in figure 30.

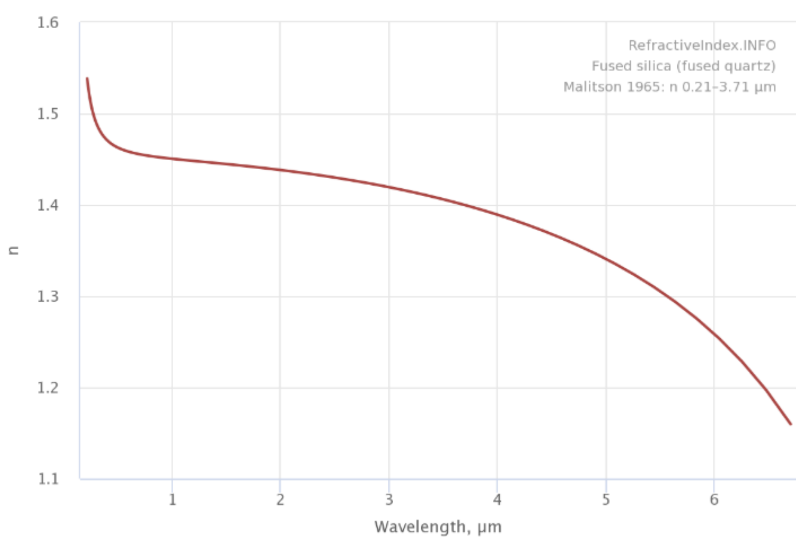

Figure 30: Refractive index vs wavelength of fused silica[26].

This results in a maximum refractive index uncertainty of 0.0005. However, for a sample undergoing stress, the value of concern is not the refractive index itself, but rather the change in refractive index due to stress. This change in refractive index is related to wavelength as shown in equation 1. Plugging in the boundary wavelengths, we get a birefringence uncertainty of about ±1.5%, which directly correlates to a retardance uncertainty of ±1.5% as well. This assumes all wavelengths transmit equally. However, the central wavelength has the highest transmission rate, with transmission decreasing as wavelength deviates from the central value, meaning this uncertainty is likely an overestimate. Another point of concern is the camera clocking procedure. The BX-51 microscope is used in multiple configurations with different cameras. As such the Lucid Triton DoFP camera must be remounted with each use. As orientation of the linear polarizers in the focal plane is a key component of the data processing, this orientation must be configured in the exact same manner for every measurement. To achieve this, the circular polarizer is removed and the partial polarization from the fold mirror is measured while the camera is actively rotated. As shown in figure 31, the average polarization intensity for each of the grids of linear polarizers is recorded, and the camera is rotated such that the 0° polarization is maximized and the intensities of the 45° and 135° linear polarizations are equal.

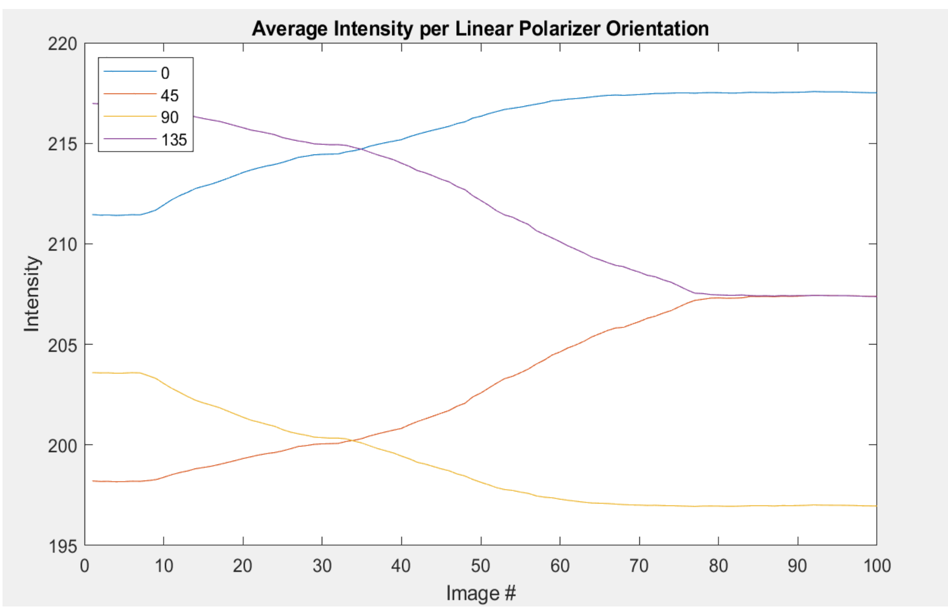

Figure 31: Average intensities of each of the four linear polarizer grids on the DoFP camera as the camera is rotated to achieve a consistent imaging orientation for each measurement.

Due to the geometry of the mirror, light is partially polarized along the 0° direction after reflection. Therefore, if the 0° linear polarizers in the camera polarizer grid are oriented along this same direction, then the maximum intensity of this orientation should be achieved for that set of pixels. Any deviation from this position will lead to uncertainty in the retardance orientation results. Furthermore, when the circular polarizer is placed into the system, it must be positioned in the same way each time. This is due to the interaction between the circular polarizer and the partially linearly polarized output from the mirror. Although light is ideally entirely circularly polarized at the output of the circular polarizer regardless of orientation, because a circular polarizer consists of a linear polarizer in series with a quarter wave plate, there will be varying levels of diattenuation between the mirror output and the linear polarizer depending on the circular polarizer orientation. This would result in varying intensities across multiple imaging sessions, convoluting result comparisons. Furthermore, the circular polarizer does not produce perfectly circularly polarized light, but rather produces elliptically polarized light that is close to left hand circular polarization. Therefore, it is important to precisely orient this component in the same manner for each imaging session to improve repeatability. Finally, it is of value to note that rotation of the circular polarizer also leads to slight image translation, suggesting that there is some wedge in the circular polarizer component. This causes undesired background retardance measurement as calculations assume the output to be perfectly linearly polarized. Moving forward to the objective, it is important to recognize that even at low values of NA, there is still some angle of illumination acceptance that should be noted. The smallest possible NA achievable using the BX-51 aperture stop is 0.05, which corresponds to a maximum angle of acceptance of about 2.9°.

$$\mathrm{NA} = n * \sin(\theta) \tag{43}$$

For a 0.5 mm thick sample with a laser-induced modification along the midplane of the sample, this causes an area of uncertainty with a 12.66 µm radius at either end of the sample directly above or below the modification as shown in figure 32.

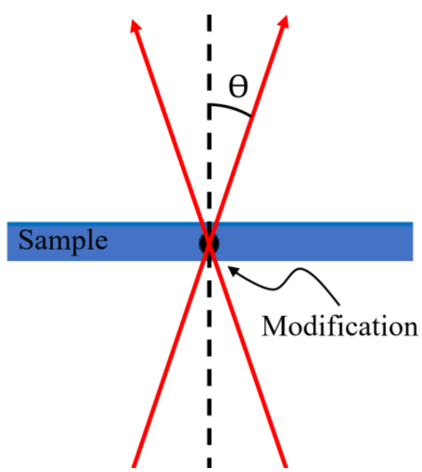

Figure 32: Representation of area of uncertainty above and below the plane of measurement due to illumination angle of acceptance.

In order to reduce result uncertainty, measurements should be made on modifications with only unmodified material above and below them within this area, as any additional modifications within this radius at some depth below the measured modification will contribute to the retardance measured for some of the rays passing through the modification of interest. It may also be possible to alter the aperture stop of the microscope to further decrease NA. However, at some point the procedure will be limited by photon count once NA is substantially decreased. Another previously mentioned cause of uncertainty is the many sources of noise in the system contributing to the intensity fluctuation of about 8 counts. However, by averaging the retardance magnitude and orientation for 50 images over a short period, this noise is reduced, but not entirely eliminated. The most interesting source of result uncertainty comes from the DoFP camera itself. As each super-pixel is covered by a 4x4 grid of linear polarizers, one would expect that the recorded intensity for each of the polarization outputs to be the same if the input light is completely unpolarized. However, when imaging an opal diffuser, the average intensity for some polarization orientations was greater than that of others. If this were due to some diattenuation or retardance caused by the microscope components, then a rotation of the camera would reveal fluctuating intensity measurements, as the transmitted polarization state of each of the four polarization orientations would rotate as well. However, as shown in figure 33, the change in intensity with rotation for each of the polarization orientations in the DoFP camera is exceptionally low compared to the relative intensities between each orientation.

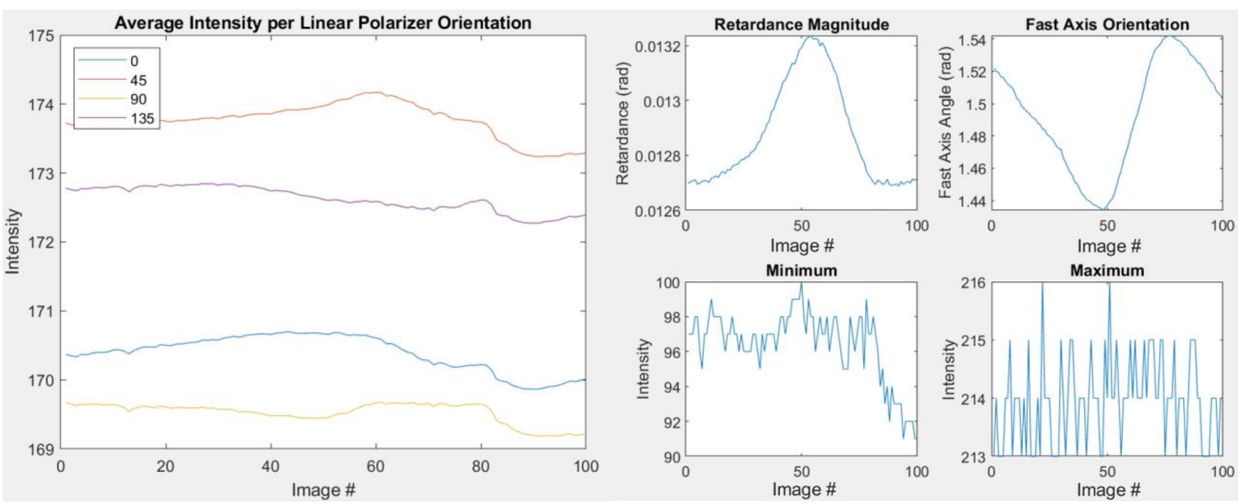

Figure 33: (Left) Average intensity recorded by each grid of linear polarizers oriented along a particular direction. Images were taken while the camera was manually rotated up to 180°, such that each polarizer grid passed through every possible orientation while imaging an opal diffuser. (Right) Retardance magnitude and orientation used to characterize degree of uncertainty. Minimum and maximum intensity values are displayed to avoid both over and under saturation.

This suggests that on average, some grids of polarizers perform better than others in terms of diattenuation, which results in an inherent recorded system retardance magnitude fluctuation due to camera orientation of 0.0005 radians and total retardance of about 0.013 radians. However, in order to reduce these values, a scalar mask can be applied to each grid of pixels such that the output intensity for unpolarized light is the same for each polarization orientation. A scalar mask was made by taking the average intensity over a particular pixel for an extended period of time, and then dividing that by the expected intensity. After applying the scalar mask to the entire image, the camera was again rotated 180° and the average intensity across each grid of polarizers was recorded as shown in figure 34.

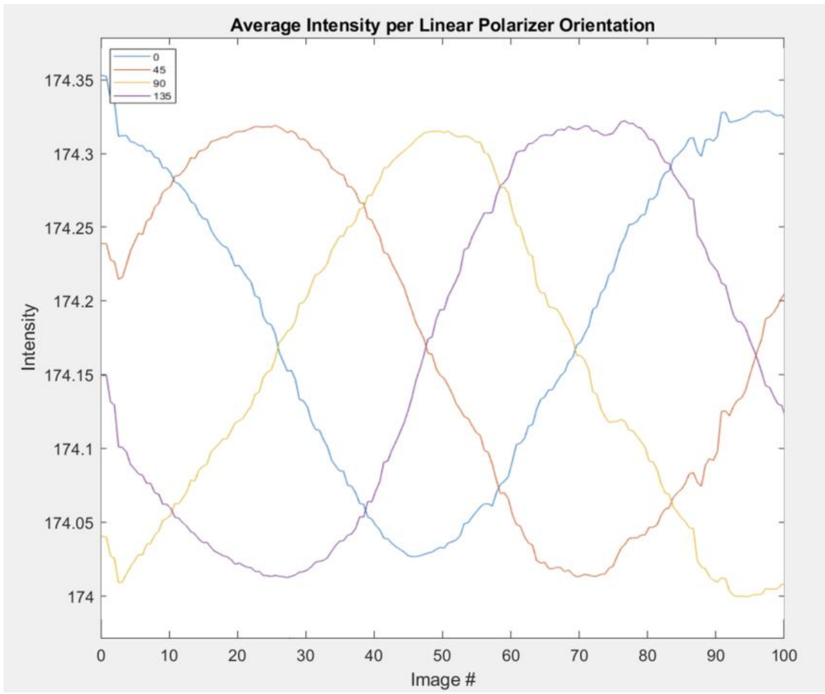

Figure 34: Average intensity recorded by each grid of linear polarizers oriented along a particular direction while imaging an opal diffuser during manual camera rotation.

Applying the scalar mask essentially eliminated retardance fluctuation due to camera rotation as the diattenuation of each wire grid polarizer was scaled appropriately. However, there are clearly still polarization effects present in the microscope between the sample and detector as can be seen by the change in output intensity with camera angle. As the linear polarizers are oriented at 0°, 45°, 90°, and 135°, the phase difference of $\frac{\pi}{4}$ between each when rotated through 180° is entirely expected when some amount of polarization is present in the system. While this leads to additional retardance in measured data, the calibration technique described in section 2.2 largely eliminates this effect. A simple method to test this statement is to place a linear polarizer in the focal plane of the imaging polarimeter. Assuming light is perfectly linearly polarized at the output of the linear polarizer, a retardance of $\frac{\pi}{2}$ should be recorded. This is because a quarter wave plate oriented at ±45° is used to convert circularly polarized light to linearly polarized light. While a linear polarizer is actually a diattenuator, the imaging polarizer uses intensity data to output retardance magnitude and orientation, as it is assumed that no diattenuation is present in the measured sample. While this is generally true for imaging stress birefringence, such an assumption can be taken advantage of here to evaluate the effectiveness of the calibration technique in eliminating polarization effects due to microscope elements. Figure 35 demonstrates the results for placing a linear polarizer oriented at 0° degrees in the imaging plane.

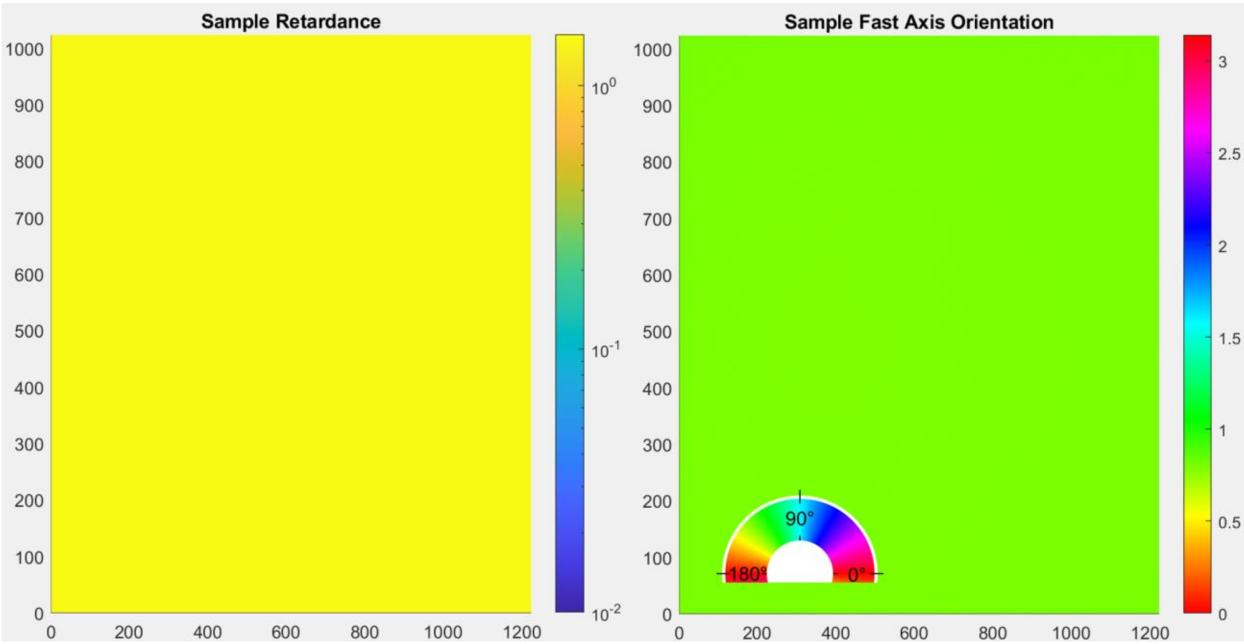

Figure 35: (Left) Retardance magnitude measured when a linear polarizer is placed in the focal plane of the imaging polarimeter. (Right) Retardance fast axis orientation for the same sample. Color values are in radians.

A retardance of nearly $\frac{\pi}{2}$ was measured over the entire focal plane with the exception of 1 pixel. The outlier data from that single pixel is likely due to a failure or manufacturing error of the pixel or wire grid polarizer associated with that pixel. This demonstrates that the extinction ratio of the linear polarizers in the detector plane oriented perpendicular to the axis of transmission of the sample polarizer is great enough such that, in reference to equations 29 and 30, the final "A" parameter was -1 and the final "B" parameter was 0 for this sample polarizer orientation. Furthermore, as this experiment was repeated at a variety of sample polarizer orientations with the same retardance magnitude results, this demonstrates the effectiveness of our background calibration technique in removing retardance or diattenuation effects due to exterior components. The retardance orientation was also consistent with expectations, however, while the RMS error associated with retardance magnitude was 0.0001 radians, the retardance orientation RMS error was 0.009 radians or 0.5°. While these results suggest the retardance orientation and magnitude of a laser-induced modification made at 980 kHz, with a power of 2820 nJ, and consisting of 20 laser pulses should be measurable, until the aforementioned artifacts produced during modification generation can be eliminated, the stresses resulting from the modification itself cannot be extracted using this current technique.

Chapter 5 – Summary and Future Prospect

The aim of this thesis was to demonstrate the design and theory of an imaging polarimeter that can be used to characterize the magnitude and orientation of principal stresses in fused silica from laser pulse induced modifications. Ultimately the proposed tool will be used to understand the extent of stress fields from these modifications on a micro-scale using retardance magnitude and orientation measurements, such that the interactions between individual laser-induced modifications can be better understood. The mathematical derivation relating to the retardance magnitude and orientation, and the relationship between these quantities and the generated principal stresses has been demonstrated as well. While the imaging polarimeter was successfully constructed, there are still many methods and potential alterations that can be implemented to improve results as discussed in section 4.2. Furthermore, a qualitatively accurate finite element analysis was performed to demonstrate the predicted birefringence behavior of laser pulse induced modifications. This analysis can also be used in the future to explore the non-equibiaxial stress contributions due to laser polarization orientation, as well as the form birefringence from generated nanogratings. The correlation between this form birefringence and laser polarization orientation can also be explored. Understanding these interactions can lead to improved precision of the ULSF process through a better understanding of the stress interactions at the micro-scale. In the future, a comparison between average measured stresses across the entire sample and stresses at the micro-scale can also be compared to potentially verify stress measurement methods. While an exact comparison between experimental and simulated results has not yet been possible for the proposed use case, the groundwork for such a comparison has been laid through the creation of both the physical polarimeter and the finite element model. Such a comparison will become possible if either the polarimeter retardance magnitude resolution can be improved, or modifications with high energy and pulse number can be made such that the generated retardance field is large enough to be accurately measured.

References

1. B. D. Chalifoux, K. A. Laverty, and I. J. Arnold, "Ultrafast laser stress figuring for accurate deformation of thin mirrors," Opt. Express **30**(11), 17767–17780, Optica Publishing Group (2022) [doi:10.1364/OE.456679].
2. R. R. Gattass and E. Mazur, "Femtosecond laser micromachining in transparent materials," 4, Nat. Photonics **2**(4), 219–225, Nature Publishing Group (2008) [doi:10.1038/nphoton.2008.47].
3. T. Brabec and F. Krausz, "Intense few-cycle laser fields: Frontiers of nonlinear optics," Rev. Mod. Phys. **72**(2), 545–591, American Physical Society (2000) [doi:10.1103/RevModPhys.72.545].
4. T. Mura, *Micromechanics of defects in solids*, Springer Netherlands, Dordrecht (1987) [doi:10.1007/978-94-009-3489-4].
5. R. Taylor, C. Hnatovsky, and E. Simova, "Applications of femtosecond laser induced self-organized planar nanocracks inside fused silica glass," Laser Photonics Rev. **2**(1–2), 26–46 (2008) [doi:10.1002/lpor.200710031].
6. R. Chipman, W. S. T. Lam, and G. Young, *Polarized Light and Optical Systems*, CRC Press, Boca Raton (2018) [doi:10.1201/9781351129121].
7. E. Bricchi, B. G. Klappauf, and P. G. Kazansky, "Form birefringence and negative index change created by femtosecond direct writing in transparent materials," Opt. Lett. **29**(1), 119–121 (2004) [doi:10.1364/ol.29.000119].
8. D. Hemsley, "33 - Optical Microscopy," in Comprehensive Polymer Science and Supplements, G. Allen and J. C. Bevington, Eds., pp. 765–784, Pergamon, Amsterdam (1989) [doi:10.1016/B978-0-08-096701-1.00033-1].
9. J. Canning et al., "Anatomy of a femtosecond laser processed silica waveguide [Invited]," Opt. Mater. Express **1**(5), 998–1008, Optica Publishing Group (2011) [doi:10.1364/OME.1.000998].
10. E. Arbabi et al., "Full-Stokes Imaging Polarimetry Using Dielectric Metasurfaces," ACS Photonics **5**(8), 3132–3140, American Chemical Society (2018) [doi:10.1021/acsphotonics.8b00362].
11. "Olympus BX51 Fluorescence Microscope Cutaway Diagram | Olympus LS," <https://www.olympus-lifescience.com/en/microscope-resource/primer/techniques/fluorescence/bx51fluorescence/> (accessed 29 March 2023).
12. "632nm CWL, 10nm FWHM, 50mm Mounted Diameter | Edmund Optics," <https://www.edmundoptics.com/p/632nm-cwl-10nm-fwhm-50mm-mounted-diameter-/29036/> (accessed 24 March 2023).
13. Dave3457, *English: This circularly polarized light is considered left-handed as viewed from the receiver and right-handed as viewed from the source. (Refer here)*.
14. B. Bai et al., "Pathological crystal imaging with single-shot computational polarized light microscopy," J. Biophotonics **13**(1), e201960036 (2020) [doi:10.1002/jbio.201960036].
15. T. Tkaczyk, "Kohler Illumination," Field Guide Microsc. **FG13**, 43–45, SPIE (2010) [doi:10.1117/3.798239.ch40].
16. "Light up your life with Köhler Illumination!," Teledyne Photometrics, <https://www.photometrics.com/learn/microscopy-basics/kohler-illumination-2> (accessed 28 March 2023).
17. "Anatomy of a Microscope - Numerical Aperture and Resolution | Olympus LS," <https://www.olympus-lifescience.com/en/microscope-resource/primer/anatomy/numaperture/> (accessed 28 March 2023).
18. M. J. Katz et al., "Highly Birefringent Materials Designed Using Coordination Polymer Synthetic Methodology," Angew. Chem. **119**(46), 8960–8963 (2007) [doi:10.1002/ange.200702885].
19. R. Chipman and A. Peinado, "The Mystery of the Birefringent Butterfly," Opt. Photonics News **24**(10), 52–57, Optica Publishing Group (2013) [doi:10.1364/OPN.24.10.000052].

20. M. Shribak and R. Oldenbourg, “Techniques for fast and sensitive measurements of two-dimensional birefringence distributions,” Appl. Opt. **42**(16), 3009–3017, Optica Publishing Group (2003) [doi:10.1364/AO.42.003009].
21. K. Schwertz, “Useful Estimations and Rules of Thumb for Optomechanics,” 2010.
22. “Mechanical Stress and Optics,” in Integrated Optomechanical Analysis, Second Edition, Society of Photo-Optical Instrumentation Engineers (2012) [doi:10.1117/3.974624.ch8].
23. K. E. Cramer, M. Hayward, and W. T. Yost, “Quantification of residual stress from photonic signatures of fused silica,” AIP Conf. Proc. **1581**(1), 1679–1686, American Institute of Physics (2014) [doi:10.1063/1.4865025].
24. “Trans - the figure - Transformation of Stresses and Strains David Roylance Department of Materials - Studocu,” <https://www.studocu.com/row/document/%E5%B9%BF%E4%B8%9C%E4%BB%A5%E8%89%B2%E5%88%97%E7%90%86%E5%B7%A5%E5%AD%A6%E9%99%A2/physic/trans-the-figure/38783235> (accessed 30 March 2023).
25. B. McMillen and Y. Bellouard, “Direct-write diffracting tubular optical components using femtosecond lasers,” SPIE LASE **8972** (2014) [doi:10.1117/12.2042662].
26. I. H. Malitson, “Interspecimen Comparison of the Refractive Index of Fused Silica*,†,” J. Opt. Soc. Am. **55**(10), 1205 (1965) [doi:10.1364/JOSA.55.001205].